REDUCED MODELING OF LOW-TEMPERATURE GAS DISCHARGES IN GLOW MODE

by

ESTEBAN CISNEROS

Presented to the Faculty of the Graduate School of
The University of Texas at Arlington in Partial Fulfillment
of the Requirements
for the Degree of

MASTER OF SCIENCE IN AEROSPACE ENGINEERING

THE UNIVERSITY OF TEXAS AT ARLINGTON

December 2014

to Martha

ACKNOWLEDGEMENTS

This work would not have been possible without the constant support, encouragement and intellectual input of Dr. Luca Massa, who has always been there to help me. Most imporantly however, he has taught me that academic research is fun and exciting, and that I am capable of performing at a high level. I would also wish to address special thanks to Dr. Marie Denison, who taught me so much about plasma physics, being a great mentor, collaborator and friend.

I am also grateful towards my academic advisor Dr. Atilla Dogan and professor Dr. Zhen Han, members of the examination committee, for their time and dedication reviewing the present work. I would also like to thank them for their inspiring and entertaining lectures in flight mechanics and gas dynamics, respectively.

Furthermore, I would like to acknowledge the financial support granted by Mexico's National Council of Science and Technology (CONACYT) and the computational resources provided by the Texas Advance Computing Center (TACC).

Finally, this thesis is dedicated to my parents Carlos and Monica, and my future wife Martha, who have accompanied me through this wonderful journey of discovery. It is through their love that I have overcome so many obstacles to reach my goals and dreams. I am forever in debt.

October 16, 2014

ABSTRACT

REDUCED MODELING OF LOW-TEMPERATURE GAS DISCHARGES IN GLOW MODE

Esteban Cisneros, M.S.

The University of Texas at Arlington, 2014

Supervising Professor: Luca Massa

Gas discharge actuation of fluid dynamics phenomena has garnered significant attention in recent years due to their low-power requirements and their geometrical simplicity, amongst others. However, many of their actuation mechanisms and physical couplings are still not well-understood, calling for numerical efforts to address many of these problems. Modeling and simulation of plasma-flow interaction is an exhaustive task because of the multi-physics, multi-scale nature of the problem. One particular concern is the appropriate modeling of the discharge detailed chemistry in order to reduce the computational cost associated with it while capturing all of its finest features.

Modern reduction techniques attempt to create reduced-order models of chemical kinetics by identifying low-dimensional invariant attractors in phase space. These attractors, or some forms of approximation, are parametrized and stored with the intention of retrieval in time-intensive multiscale, turbulent, CFD simulations. Two popular rational reduction techniques are applied to several electrical discharge systems in noble gases after addressing their appropriate modeling with the intention

of studying the structure and character of their one-dimensional invariant attractor under a wide range of reduced electric fields. It is shown that the branches of the manifold correspond to high and low ionization states and that a particular attractor exists for a small range of low reduced fields. This is of great importance to the modeling of flow actuation chemistry. Finally, it is demonstrated that electron runaway is analogous to radical explosion in combustion.

TABLE OF CONTENTS

LIST OF ILLUSTRATIONS

LIST OF TABLES

CHAPTER 1

INTRODUCTION

Plasma flow actuators have garnered significant attention in recent years as potential candidates for assisting in boundary layer transition control, thrust generation, combustion mixing and ingition enhancement, amongst others [4–7]. These actuators, when operating in glow discharge mode, generate nonequilibrium weakly-ionized plasmas, which are preferred over the thermal plasmas generated by arc discharges, due to their relative low power demand. A nonequilibrium, or non-thermal, weakly-ionized plasma is that in which the ion and background gas temperatures remain close at around room temperature but differ significantly from electron temperatures, usually at 1-10 eV. The discharge occurs when a sufficiently large electric field is applied by two separate electrodes to a gas such that charged particles are created in electron-impact ionization. Ions and neutral particles collide, and thus momentum and heat are transferred from the plasma to the background gas.

Of particular interest are dielectric barrier discharge (DBD) actuators, which have shown promising flow-control capabilites [8–10]. These consist of top and bottom electrodes separated by a dielectric material, which generate plasma in a self-limiting process. Ionization occurs over the exposed electrode towards the covered electrode when either high enough AC or pulsed voltages are applied. Surface charge accumulation reduces the potential difference and thus terminates any further plasma emission until the next AC cycle. The discharge's structure is streamer-like during

electrode positive polarity and diffusive during negative polarity and the base flow is modified by momentum transfer. Another type of popular plasma flow actuator is the surface direct currect discharge (DCD) actuator. This actuator generates a dominant Joule heating effect and its actuation mechanism, i.e. the Townsend mechanism, is simpler than that of a DBD actuator. This configuration consists of the two electrodes flush mounted onto the surface, and when a high enough DC voltage is applied between them, the gas is heated [11, 12].

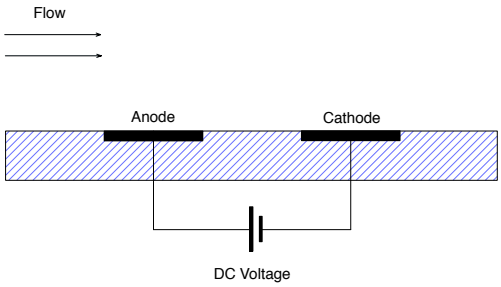

Figure 1.1: Typical configuration of a DCD actuator.

Numerous recent flow control techniques based on DBD actuators, such as pitch and roll control, have been investigated experimentally and numerically [13,14]. Furthermore, DBD actuators can modify a boundary layer by introducing optimal perturbations or by changing its receptivity. The first approach is appropriate for lower speed regimes because of its lower power demands and was shown to be effective in amplified fluid systems [15]. The second approach, known as subcritical forcing, requires careful matching between the forcefield lengthscale and the most receptive region in order to reduce power demands. Compressibility effects on actuation by such discharges result in a deeper excitation of the boundary layer. As the Mach

number increases, the receptive region penetrates into the boundary layer [16]. However, the interaction of supersonic flows with weakly-ionized plasmas, their chemistry, interactions with shocks, actuation mechanisms and their operational mode transition is yet to be completely understood.

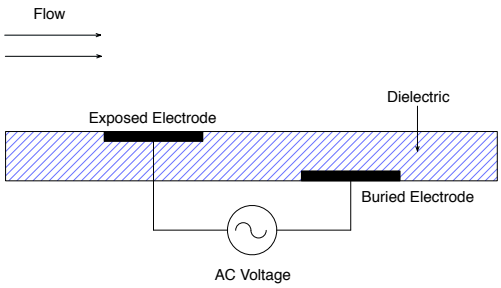

Figure 1.2: Typical configuration of a DBD actuator.

Numerical studies of plasma discharges are typically based on moments of the Boltzmann equation, being the most computationally viable alternative. Yet, these continuum models tend to be very stiff due to disparate timescales and lengthscales. Even more so, depending on the application, these models are coupled with at least the Poisson equation and at most the full set of Maxwell Equations. A comprehensive treatment of numerical modeling of plasma discharges is given in ref. [17]. Although some contributions to computational cost may be aliviated by parallel computing, operator splitting and novel patch adaptive mesh refinement solvers [18], the evaluation and integration of the detailed chemistry source term is very expensive, as in any reactive flow simulation [19]. A common approach to plasma chemistry has been the employment of three-species models, consisting of positive ions, electrons and neutrals [20, 21]. These are useful because they are comparable to plasma dis-

charges in noble gases, which are well understood [22]. Four species models extend this approach by including negative ions.

Discharges in atmospheric gases are commonly modeled with detailed chemistry. Kossyi et al. [23] present a large kinetic scheme of about 450 reactions for discharges in $N_2 - O_2$ air-like mixtures. This model has been reduced for numerical simulations of DBD applications either by rationally hand-picking only relevant reactions such as in [24] or by sensitivity analysis, as in [25]. Mahadevan [26] derived a reduced $N_2 - O_2$ mechanism in order to describe a surface DCD primarily from [24]. The resulting kinetic mechanisms' sizes range from 8 to 23 species and 8 to 50 reactions. Other detailed kinetic mechanisms found in the literature for discharges in air and air-like mixtures include the one used by Tsyganov and Pancheshnyi in [27] for zero-dimensional DBD's in N_2 and the one developed by Castillo et al. [28]. A complete treatment on plasma kinetics in atmospheric gases is given in ref. [29].

Modern automatic reduction techniques rely on the existence of lower dimensional invariant attracting manifolds in phase space. Trajectories bundle upon these manifolds of decreasing dimension forward in time towards physical equilibrium. Furthermore, these attractors are associated with the system's slowest timescales. Modern dimension reduction methods are generally classified in two groups: local timescale analysis methods and geometrical methods. Local timescale analysis methods reinterpret the system's timescale separation as a source of stiffness by acknowledging that fast modes relax rapidly for slow modes to govern the system's dynamics thereafter. Prominent examples of these are computational singular perturbation (CSP) method by Lam and Goussis [30] or instrinsic low-dimensional manifold (ILDM) method by Maas and Pope [1] and have been thoroughly exploited

in combustion modeling and simulation [31–33]. The ILDM method, a mathematically sound approach, approximates a stable geometrical invariant attractor with a low-dimensional manifold. This manifold is parametrized by just a few reaction progress variables, thus succesfully reducing the dimensions of the state space. Infomation can subsequently be stored and retrieved for reactive flow calculations. The method also provides information on the hierarchy of the system and can be extended to study coupling with transport processes [34, 35]. Geometrical methods are instead based upon characterizing the attractors by properties like invariance, slowness and smoothness. Amongst these methods are the invariant constrained equilibrium preimage curve (ICE-PIC) method [36] and one-dimensional slow invariant manifold (1D SIM) method by Al-Khateeb et al [37]. This recent method explores the dynamical character of the system after removing all constraints in order to generate the branches of the invariant attractor by forward propagation. It allows for a comprehensive study of the structure of the slow motions in phase space.

The application of formal reduction methods to plasma discharge kinetics has been limited, despite their success in reducing and describing hydrocarbon systems. Dauwe et al. [38] succesfully applied the ILDM method to reduce and investigate the properties of a hydrocarbon mechanism immersed in a plasma chamber. Thus, the present work is dedicated to the rational reduction of air plasma discharge kinetics. The governing equations of plasma discharges, the mathematical formalization of detailed chemical kinetics and the governing geometrical and timescale principles of the reduction methods are presented in chapter 2. Chapter 3 deals firstly with the numerical simulation of gas discharges so as to validate the models, and continues with the numerical implementation of the 1D SIM method by Al-Kahteeb et al. [37] and an efficient algorithm for computing, parametrizing and storing the ILDM. The

reduced-order models are delived and compared in chapter 4 and their peculiarities are pointed out. Chapter 5 cloncludes this thesis and states future work.

CHAPTER 2

GOVERNING EQUATIONS

One of the main complexities of reactive flow problems is their multiscale nature. Chemical processes introduce disparate timescales which, when coupled with transport timescales, significantly increase the computational cost of flow simulations. The chemistry of low-temperature discharges is no exception, as timescales usually span up to eight orders of magnitude.

This chapters presents two reduction techniques which aliviate the stiffness problem. Firstly, the equations that govern low-temperature discharges in abscense of magnetic fields are derived as moments of the Boltzmann equation. This is followed by a thorough analysis of the chemical source term. It is shown that composition evolves in a reduced subspace of the composition space. Furthermore, slow modes govern the dynamics of the system along lower-dimensional manifolds upon which trajectories merge en route to equilibrium. Finally, with this knowledge at hand, both reduction techniques are outlined, with their strengths, weakness and differences highlighted.

2.1 Plasma Discharge Continuum Model: The Moment Equations

The particle species velocity distribution function $f_s(\boldsymbol{x}, \boldsymbol{v}, t)$ is a probability density function that measures the likeliness of finding particles from species s in a differential element of six-dimensional phase space. It is normalized such that

$$\int f_s(\boldsymbol{x}, \boldsymbol{v}, t) d^3v = n_s. \tag{2.1}$$

The independent variables are particle position $\boldsymbol{x}$, particle velocity $\boldsymbol{v}$ and time t. Particle velocity can be split into average (or drift) velocity $\boldsymbol{u}$ and random (or thermal) velocity $\boldsymbol{u}'$. Relevant macroscopic properties that describe the flowfield are statistical averages, or moments, of the velocity distribution function. The $k-th$ moment ϕ_k of f_s is given by

$$\phi_k = \int m_s(\boldsymbol{v}_s)^k f_s d^3v. \tag{2.2}$$

Species mass m_s, momentum $m_s\boldsymbol{u}_s$ and total energy $\frac{1}{2}m_s(\boldsymbol{u}_s \cdot \boldsymbol{u}_s)$ are the zeroth, first and second order moments respectively, and, following (2.2), are given by:

$$m_s n_s = \int m_s f_s d^3v \tag{2.3a}$$

$$m_s n_s \boldsymbol{u}_s = \int m_s \boldsymbol{v}_s f_s d^3v \tag{2.3b}$$

$$\frac{1}{2} m_s n_s (\boldsymbol{u}_s \cdot \boldsymbol{u}_s) = \frac{1}{2} \int m_s (\boldsymbol{v}_s \cdot \boldsymbol{v}_s) f_s d^3v \tag{2.3c}$$

Another relevant moment, associated with the thermal velocity of species s, is the scalar pressure given by:

$$p_s = \int m_s (\boldsymbol{v}'_s \cdot \boldsymbol{v}'_s) f_s d^3v \tag{2.4}$$

The translational kinetic energy can be further split into drift and thermal contributions. While the former corresponds to the average particle motion, the latter is associated with the translational temperature of species s, which by close inspection is also proportional to the scalar pressure, i.e.

$$e_s = \frac{3}{2} k_B T_s \tag{2.5a}$$

$$p_s = k_B n_s T_s \tag{2.5b}$$

where k_b is the Boltzmann constant.

The Boltzmann gas kinetic equation governs the evolution of the velocity distribution function and as such, a system consisting of a Boltzmann equation for each species coupled to the Maxwell equations would yield the most meticulous representation of a plasma [39]. This approach is unviable due to its high computational cost. However, moments of the Boltzmann equation and their appropriate closures constitute a strong and accurate description of plasmas as a continuum.

The Boltzmann equation reads:

$$\frac{\partial f_s}{\partial t} + \boldsymbol{v_s} \cdot \nabla f_s + \boldsymbol{a_s} \cdot \nabla_{\boldsymbol{v}} f_s = C[f] \tag{2.6}$$

where $C[f]$ is the collision operator, which indicates the rate of change in f_s due to collisions. Eq. (2.6) describes the time evolution of particles during their trajecto-

ries in phase space. Their appearance or disappearance depends only on collisions. Charged particles are accelerated by electric and magnetic effects, i.e.

$$\boldsymbol{a}_s = \frac{z_s q}{m_s}[\boldsymbol{E} + \boldsymbol{v}_s \times \boldsymbol{B}] \tag{2.7}$$

where q is the elemetary charge and $\boldsymbol{E}$ is the electric field, determined by solving the Poisson equation for the electric potential ϕ:

$$E = -\nabla\phi \tag{2.8a}$$

$$\nabla^2\phi = -\frac{q}{\epsilon_0}\sum_{i=1}^{n_s} z_i n_i \tag{2.8b}$$

where ϵ_0 is the permittivity of the background gas.

There are two common approaches to derive the moments of eq. (2.6). The first approach consists of the direct derivation of the first three moments by applying eq. (2.2) to every term in eq. (2.6). The second approach succeeds through a generalized transport equation, where the desired moments are substituted to yield the continuum model. The resulting set of conservation laws is known as the five-moment model of plasmas as a continuum, but will be omitted here for brevity. However, this model can be found in [17], along with their derivation and a sound description of its source terms and closure models.

Assuming no magnetic effects and disregarding all inertia terms in the resulting momentum equations of the five-moment model, a two-moment model is obtained. These conservation equations are:

$$\begin{aligned} \frac{\partial}{\partial t}(m_s n_s) + \nabla \cdot (m_s n_s \boldsymbol{u}_s) &= F_s \\ n_s \boldsymbol{u}_s = n_s \boldsymbol{u}_n \pm \mu_s n_s \boldsymbol{E} - \frac{D_s}{k_B T_s} \nabla p_s & \\ \frac{\partial}{\partial t}(m_s n_s e_s) + \nabla \cdot (m_s n_s e_s \boldsymbol{u}_s) &= -\nabla \cdot \boldsymbol{H}_s - p_s \nabla \cdot \boldsymbol{u}_s + \tilde{F}_s \end{aligned} \tag{2.9}$$

where μ_s is the mobility of species s, D_s its diffusivity given by Einstein's relation, $\boldsymbol{H}_s$ is the heat flux vector given by Fourier's law and F_s and $\tilde{F}_s$ are the species and energy source terms, respectively. The flux expression is also known as the drift-difussion approximation. This approach was adopted in [26] and [4].

A one-moment model, called the local field approximation (LFA), consists of the continuity equation, the drift-diffusion approximation and an algebraic relation between the reduced field and the electron temperature, i.e.

$$f(E/N_g, T_e) = 0. \tag{2.10}$$

When employed, it is assumed that electrons are in equilibrium with the electric field, and has been used extensively, see for example [12].

2.2 Mathematical Formalism of Chemical Kinetics

Operator splitting techniques such as Godunov's split allow for direct integration of the chemical source over a half-time step $\Delta t/2$ with second order accuracy.

The final step of an operator splitting techinque consists of directly integrating the chemical source term by itself, yielding a non-linear initial value problem (IVP):

$$\frac{d\boldsymbol{\psi}}{dt} = \boldsymbol{F}(\boldsymbol{\psi}) \tag{2.11a}$$

$$\boldsymbol{\psi}(0) = \boldsymbol{\psi}_i. \tag{2.11b}$$

The resulting ODE represents a closed homogeneous system in each one of the discretized region's cells. Two further assumptions, namely that the system is also isothermal and that the LFA applies, are made to simplify modeling and computations.

Consider the n_s-dimensional composition vector $\boldsymbol{\psi} = (\psi_1, \psi_2, ..., \psi_{n_s})$ in units of kmol/m^3. The components of this vector are the specific mole numbers, but it could be extended to include electron, gas and ion temperatures, or any other passive scalar, without loss of generality. The evolution of this vector within composition space $\boldsymbol{\Psi}$ is described by mass-action kinetics, which will be outlined henceforth. Any chemical reaction mechanism of size n_r can be expressed as:

$$\sum_{s=1}^{n_s} \nu'_{sr} M_s \leftrightharpoons \sum_{s=1}^{n_s} \nu''_{sr} M_s, \;\; r = 1, 2, ..., n_r \tag{2.12}$$

where M_s is the chemical symbol of species s, ν'_{sr} is the forward stoichimetric coefficient of species s in reaction r and, similarly, ν''_{sr} is the backward stoichimetric coefficient of species s in the same reaction such that the s^{th} component ν_{sr} of the reaction vector $\boldsymbol{\nu}_r$ of reaction r is given by:

$$\nu_{sr} = \nu''_{sr} - \nu'_{sr}. \tag{2.13}$$

These vectors form a $n_s \times n_r$ reaction matrix $\boldsymbol{\nu}$. There are n_e quantities that are conserved in closed, spatially homogeneous systems, such as element composition and, as is the case in quasi-neutral plasmas, charge. These quantities can be organized in a vector $\boldsymbol{\xi}$ and are related to the composition vector through the element composition matrix $\boldsymbol{\mu}$:

$$\boldsymbol{\xi} = \boldsymbol{\mu}^T \boldsymbol{\psi}. \tag{2.14}$$

Each entry μ_{se} represents the amount of conserved quantity e in species s. Conservation of these quantities means that, given a basepoint state $\boldsymbol{\psi}_o$:

$$\boldsymbol{\xi} = \boldsymbol{\mu}^T \boldsymbol{\psi} = \boldsymbol{\mu}^T \boldsymbol{\psi}_o, \tag{2.15a}$$

$$\boldsymbol{\mu}^T \boldsymbol{\nu} = \mathbf{0}, \tag{2.15b}$$

i.e. $\boldsymbol{\mu}$ are the left eigenvectors of $\boldsymbol{\nu}$ corresponding to n_e zero eigenvalues. Therefore, $\boldsymbol{\nu}$ is rank deficient, i.e. $\text{rank}(\boldsymbol{\nu}) \leq n_s - n_e$.

Two consequences follow immediately. Firstly, composition space $\boldsymbol{\Psi}$ can be solely described by $\boldsymbol{\nu}$ or, alternatively, $\boldsymbol{\mu}$. Conservation further implies that composition evolution is restricted by eq. (2.15) to an affine subspace

$$\boldsymbol{\Xi} = \{\boldsymbol{\psi} \mid \boldsymbol{\mu}^T \boldsymbol{\psi} = \boldsymbol{\xi}, \boldsymbol{\psi} \in \boldsymbol{\Psi}\} \tag{2.16}$$

of dimensions no larger than $n_s - n_e$. Furthermore, not all possible states are actually physically realizable, and thus transistion between states is confined by species positivy, resulting in a convex polytope called the realizable region:

$$\boldsymbol{\Xi}^+ = \{\boldsymbol{\psi} \mid \psi_s \geq 0, \boldsymbol{\mu}^T \boldsymbol{\psi} = \boldsymbol{\xi}, \boldsymbol{\psi} \in \boldsymbol{\Psi}\} \tag{2.17}$$

Thus, the solution to (2.11) is of the form:

$$\boldsymbol{\psi}(t) = \boldsymbol{\psi}_o + \mathrm{m_T}\mathcal{D}\boldsymbol{z}(t) \tag{2.18}$$

where $\mathrm{m_T}$ is the total mass of the system, $\boldsymbol{z}(t) \in \boldsymbol{\Xi}$ is the reduced composition vector of dimensions no larger than $n_s - n_e$ in units of $\mathrm{mol/m^3 - kg}$ and $\mathcal{D}$ is a non-unique constant linear operator.

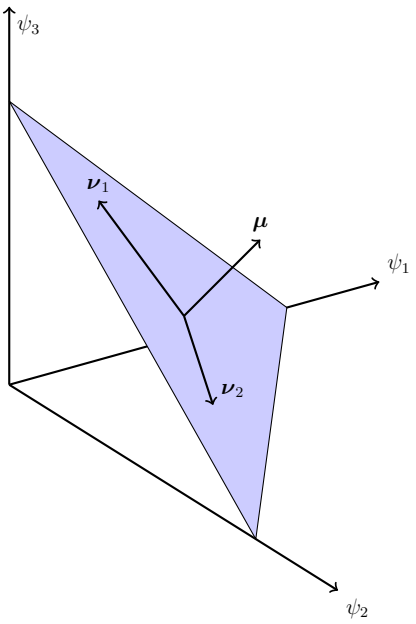

Figure 2.1: Schematic illustration of composition space for a $n_s = 3$, $n_e = 1$ system. Adapted from ref. [1].

Even though there are different ways to construct the linear operator $\mathcal{D}$, a natural option is through the singular value decomposition of $\boldsymbol{\nu}$. Consider the chemical source term in eq. (2.11), given by:

$$F_s(\boldsymbol{\psi}) = \sum_{r=1}^{n_r} \nu_{sr} \left(k_r \prod_{s=1}^{n_s} \psi_s^{\nu'_{sr}} \right) \tag{2.19}$$

i.e.,

$$\boldsymbol{F}(\boldsymbol{\psi}) = \boldsymbol{\nu} \boldsymbol{R}(\boldsymbol{\psi}) \tag{2.20}$$

where k_r is the reaction rate coefficient of reaction r and $\boldsymbol{R}(\boldsymbol{\psi})$ is the reaction rate function. By taking the singular value decomposition of the reaction matrix $\boldsymbol{\nu}$ and substituting eq. (2.20), eq. (2.11) becomes:

$$\frac{d\boldsymbol{\psi}}{dt} = \mathbf{u}\mathbf{s}\mathbf{v}^T \boldsymbol{R}(\boldsymbol{\psi}) \tag{2.21}$$

where $\mathbf{u}$ and $\mathbf{v}$ are the left and right singular vectors of $\boldsymbol{\nu}$ corresponding to its $n_s - n_e$ singular values in $\mathbf{s}$. Since both $\mathbf{u}$ and $\mathbf{v}$ are orthogonal, the above becomes:

$$\frac{d}{dt}(\mathbf{u}^T \boldsymbol{\psi}) = \mathbf{s}\mathbf{v}^T \boldsymbol{R}(\boldsymbol{\psi}) = \begin{pmatrix} \boldsymbol{f}(\boldsymbol{\psi}) \\ \mathbf{0} \end{pmatrix}, \tag{2.22}$$

but also

$$\frac{d}{dt}(\mathbf{u}^T \boldsymbol{\psi}) = \mathbf{u}^T \boldsymbol{F}(\boldsymbol{\psi}). \tag{2.23}$$

Note that $\boldsymbol{f}$ is the $n_s - n_e$ reduced chemical source term, and if

$$\mathbf{u}^T = \begin{pmatrix} \mathbf{u_r}^T \\ \mathbf{u_c}^T \end{pmatrix} \tag{2.24}$$

where $\mathbf{u_r}^T$ is the upper $(n_s - n_e) \times n_s$ block of $\mathbf{u}^T$, then from eq. (2.22)

$$\frac{d}{dt}(\mathbf{u_r}^T \boldsymbol{\psi}) = \boldsymbol{f}(\boldsymbol{\psi}). \tag{2.25}$$

Finally, by differentiating eq. (2.18) in time:

$$\frac{d}{dt}(\mathcal{D}^+ \boldsymbol{\psi}) = \mathrm{m_T} \frac{d\boldsymbol{z}}{dt} \tag{2.26}$$

where $\mathcal{D}^+$ is the right inverse of $\mathcal{D}$. By comparing the above with eq. (2.25), not only can $\mathcal{D}$ be fully defined, but also an evolution equation for the reduced composition $\boldsymbol{z}$ can be found. Knowing that,

$$\mathcal{D} = \mathbf{u_r} \tag{2.27a}$$

$$\mathcal{D}^+ = \mathcal{D}^T = \mathbf{u_r}^T \tag{2.27b}$$

and by eq. (2.23) it results that

$$\frac{d\boldsymbol{z}}{dt} = \boldsymbol{f}(\boldsymbol{z}) \tag{2.28}$$

where

$$\boldsymbol{f}(\boldsymbol{z}) = \frac{1}{m_T} \mathcal{D}^T \boldsymbol{F}(\boldsymbol{\psi}). \tag{2.29}$$

The second consequence of (2.15) pertains to the eigenspectra of both physical and reduced systems. The jacobian $\boldsymbol{F}_{\boldsymbol{\psi}}$ of the physical system (2.11) reads:

$$\boldsymbol{F}_{\boldsymbol{\psi}} = \frac{\partial \boldsymbol{F}}{\partial \boldsymbol{\psi}} = \boldsymbol{\nu} \frac{\partial \boldsymbol{R}}{\partial \boldsymbol{\psi}} = \boldsymbol{\nu} \boldsymbol{R}_{\boldsymbol{\psi}} \tag{2.30}$$

such that, by (2.15), $\boldsymbol{\mu}$ are also the left eigenvectors of $\boldsymbol{F_\psi}$ corresponding to n_e zero eigenvalues. Its eigenspectrum is then the union of two separate sets:

$$\begin{aligned} \sigma_1(\boldsymbol{F_\psi}) &= \{\overset{n_e}{0, ..., 0}\} \\ \sigma_2(\boldsymbol{F_\psi}) &= \{\overset{n_s-n_e}{\lambda_{n_e+1}, ..., \lambda_{n_s}}\} \\ \sigma(\boldsymbol{F_\psi}) &= \sigma_1 \cup \sigma_2. \end{aligned} \tag{2.31}$$

Thus, $\boldsymbol{F_\psi}$ is rank deficient, i.e. $\text{rank}(\boldsymbol{F_\psi}) \leq n_s - n_e$. This means that finding steady state conditions, i.e. physical equilibrium, which is key to the construction of low-dimensional manifolds, is not a quite straigh-forward task. Conventional tools such as Newton's method are not so readily applicable. However, the jacobian $\boldsymbol{f_z}$ of the reduced system (2.28)

$$\boldsymbol{f_z} = \frac{\partial \boldsymbol{f}}{\partial \boldsymbol{z}} = \frac{\partial \boldsymbol{f}}{\partial \boldsymbol{\psi}} \frac{\partial \boldsymbol{\psi}}{\partial \boldsymbol{z}} = \mathcal{D}^T \boldsymbol{F_\psi} \mathcal{D} \tag{2.32}$$

is obtained by a similarity transformation of the physical jacobian, and its eigenspectrum can be shown to be:

$$\sigma(\boldsymbol{f_z}) = \sigma_2, \tag{2.33}$$

such that the reduced system (2.28) inherits the timescale structure from the physical system (2.11), since timescale τ_i is realted to the eigenvalue λ_i by:

$$\tau_i = \frac{1}{|\lambda_i|}. \tag{2.34}$$

Nevertheless, the reduced system is non-singular. This proves an advantage, as will be shown, in order to construct reduce models for chemically reactive systems in

general and plasma discharges in particular.

2.3 Reduced Models for Chemically Reactive Flows

This section builds upon the previously described properties of a closed homogeneous reactor in order to provide the necessary tools for lower-dimensional manifold construction. After a discussion on the dynamical character of the non-linear reactive system, the method for constructing a one-dimensional slow invariant manifold (1D-SIM) by generating heteroclinic orbits is presented. Finally, the classical method of instrinsic low dimensional manifolds (ILDM) by Maas and Pope of approximating the invariant attractor by a local timescale analysis is revisited yet again.

2.3.1 Fast and Slow Dynamics

It has been shown that the evolution of the composition $\boldsymbol{\psi}$ of a mixture is restricted to a lower-dimensional subspace of composition space $\boldsymbol{\Psi}$. This is already advantageous, but the question remains as to how the latter evolves within the former. If chemical reactions are thought of as trajectories in phase space, certain geometrical trends can be identified. The chemical source term usually introduces a wide range of timescales, causing severe stiffness associated with reactive flow problems. However, the sparsity between timescales also forces an anisotropic phase volume contraction: trajectories in phase space relax upon successively lower-dimensional manifolds until they reach physical equilibrium, a zero-dimensional manifold. Movement along these lower-dimensional attractors is governed by slow modes, such that as soon as trajectories bundle upon them, fast transients exhaust [40]. Physically,

this means that some species are in quasi-steady state and some reactions in partial equilibrium. Hence, the key idea behind mechanism reduction consists of capturing the system dynamics by modeling the fastest timescales instead of resolving them. The dimension up to which the manifold is to be modeled is determined by the coupling with transport timescales [41].

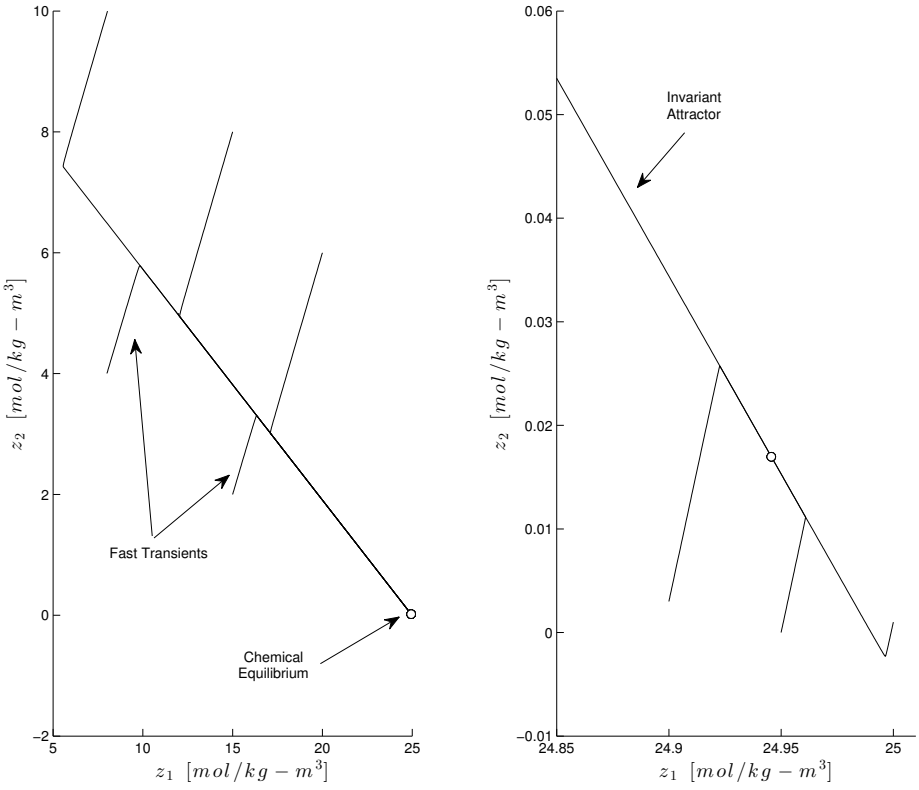

Figure 2.2: Phase diagrams of a discharge simulation in Ar as per appendix A, clusters 1 and 2, with operating conditions 3.1. Trajectories bundle upon a one-dimensional attractor in phase space.

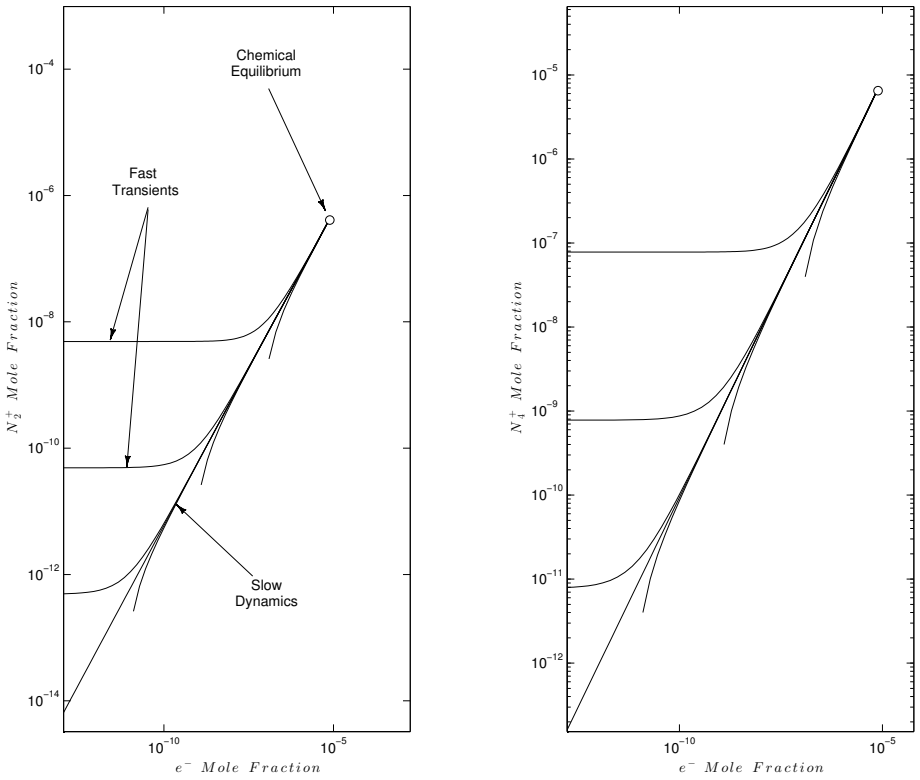

Figure 2.3: Phase diagrams of a discharge simulation in N_2 as per appendix A, with operating conditions 3.1. Trajectories bundle upon a one-dimensional attractor in phase space. This behavior is not only observable in reduced space, but also in composition space.

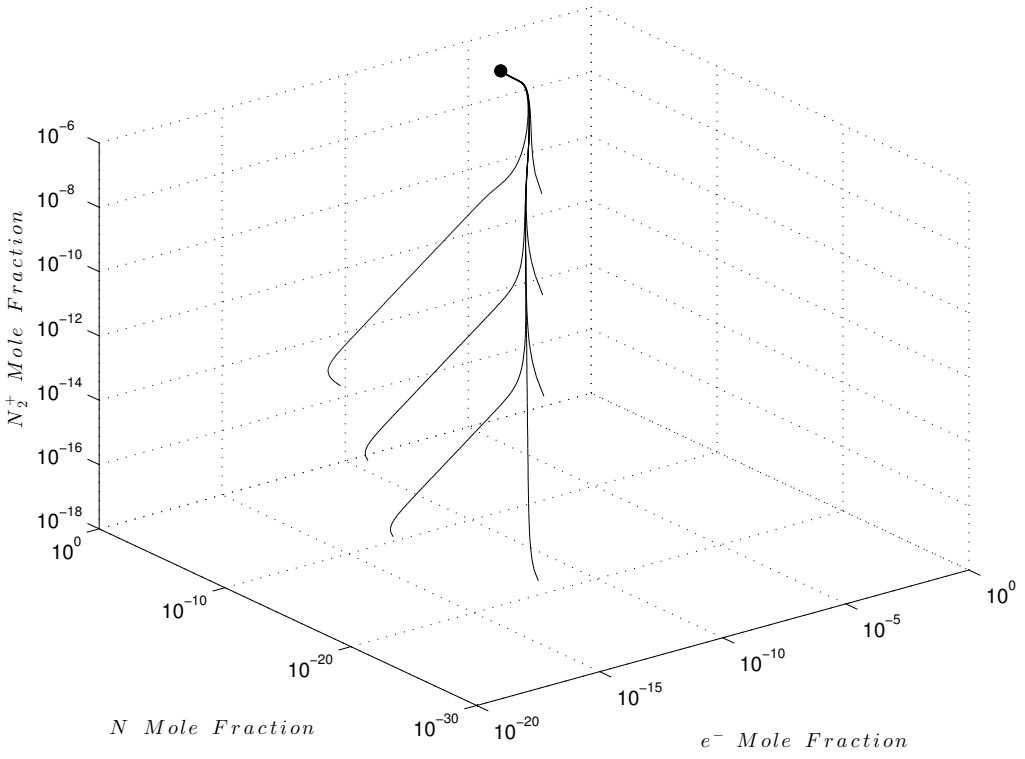

Figure 2.4: Phase diagrams of a discharge simulation in N_2 as per appendix A, with operating conditions 3.1. Trajectories bundle upon a one-dimensional attractor in phase space. This behavior is not only observable in reduced space, but also in composition space.

2.3.2 Slow Invariant Manifold

Geometrically, a SIM is an invariant manifold on which slow dynamics govern and which is attractive along its entirety [42]. Constructively, and based on the conjecture put forth by Al-Khateeb et al. [37], the SIM is a heteroclinic orbit of at most two branches, which connect unphysical to physical equilibria. By anisotropic phase volume contraction, reactive systems present SIMs of different dimensions, determined by the number of dominant slow modes. Nearby trajectories are attracted to the SIM and fast transient decay rapidly. Indeed, it is by finding or approximating the SIM that the mechanism reduction problem is effectively solved.

2.3.2.1 Geometrical Properties of the SIM

There has been substantial disagreement on the definition of slow invariant manifolds in the past [43]. However, Creta et al. [44] provide a strong geometrical definition of the 1D SIM based on global properties for two dimensional phase spaces, and extend it to larger systems and manifolds in [45]. The authors acknowledge that the most common properties of a SIM are invariance and exponential attractiveness, and formalize their definition with a sound mathematical treatment of slowness and the decay ratio of normal-to-tangential perturbations along the manifold. Some of these properties will be briefly addressed below.

An invariant manifold (IM) $\mathcal{M} \subset \boldsymbol{\Xi}$ is defined as follows. Consider the reduced reactive system (2.28) with initial condition $\boldsymbol{z}_i \in \mathcal{M}$ and solution $\overline{\boldsymbol{z}}(t)$. $\mathcal{M}$ is said to be invariant if $\overline{\boldsymbol{z}}(T) \in \mathcal{M}$ for a small $T > 0$. This is equivalent to the source term vector $\boldsymbol{f}$ being tangent to $\mathcal{M}$. Invariance thus refers to the tangency of $\boldsymbol{f}$ to the

manifold along its entirety.

Attractiveness is a key geometrical property of the SIM. For the sake of simplicity, attractiveness will be given as in [37]. An invariant manifold is exponentially attractive everywhere if:

$$\begin{gathered} \frac{|\lambda_s|}{|\lambda_i|} < 1 \\ \lambda_i < 0 \\ \{\lambda_s, \lambda_i\} \in \sigma_2,\ i = 2, ..., (n_s - n_e) \end{gathered} \tag{2.35}$$

where λ_s is the the most positive eigenvalue (and by the above also the slowest) and λ_i every other negative eigenvalue of (2.32) at $\boldsymbol{z}_{eq}$.

A IM is also 1D slow if it is associated with the system's slowest timescale. By the Hartman-Grobman theorem [46], the behavior of the non-linear system (2.28) around a critical point of $\boldsymbol{f}$ (see sec. 2.3.2.2), $\boldsymbol{z}_{eq}$, is identical to that of its linearized system:

$$\frac{d\boldsymbol{z}}{dt} = \boldsymbol{f}_{\boldsymbol{z}}(\boldsymbol{z}_{eq})(\boldsymbol{z} - \boldsymbol{z}_{zeq}). \tag{2.36}$$

Thus, as is the case with linear systems, the 1D SIM at $\boldsymbol{z}_{eq}$ will be tangent to the slowest eigenspace given by:

$$E^s = \text{span}(\mathbf{v}_s) \tag{2.37}$$

where $\mathbf{v}_s$ is the eigenvector associated with the slowest eigenvalue λ_s in σ_2. This vector is obtained by an eigendecomposition of the jacobian at $\boldsymbol{z}_{eq}$:

$$\boldsymbol{f}_z(\boldsymbol{z}_{eq}) = \mathbf{V}\ \mathbf{\Lambda}\ \mathbf{V}^{-1} = \begin{pmatrix} \mathbf{v}_s & \mathbf{V}_f \end{pmatrix} \begin{pmatrix} \lambda_s & 0 \\ 0 & \mathbf{\Lambda}_f \end{pmatrix} \begin{pmatrix} \tilde{\mathbf{v}}_s^T \\ \tilde{\mathbf{V}}_f^T \end{pmatrix}. \tag{2.38}$$

If $\lambda_s > 0$ and all other eigenvalues in $\mathbf{\Lambda_f}$ are negative, then E^s is said to be unstable. On the other hand, if all the eigenvalues in σ_2 are negative, then E^s is said to be stable. Therefore, geometrical slowness of a 1D SIM is an asymptotic behaviour. A 1D SIM $\mathcal{M}_1^s$ is an IM which asymptotically converges to the system's equilibria tangentially to their slowest eigenspace E^s as $t \to \pm\infty$. Specifically, a 1D SIM converges to physical equilibrium as $t \to \infty$ and to those unphysical equlibria with an unstable slowest eigenspace E^s spanned by the slowest eigenvector $\mathbf{v}_s$ as $t \to -\infty$.

Now consider the solution $\mathcal{F}(\boldsymbol{z}_i, t)$ to the nonlinear system (2.28), where $\boldsymbol{z}_i$ is its initial condition. Function $\mathcal{F}$ is known as the system's flow. By all of the above and in the spirit of [36], the 1D SIM is thus defined by

$$\mathcal{M}_1^s = \{\boldsymbol{z} \mid \boldsymbol{z} = \mathcal{F}'(\boldsymbol{z}_{eq}, t), t \geq 0, \boldsymbol{z}_{eq} \in \partial\mathcal{M}_1^s\} \tag{2.39}$$

where $\boldsymbol{z}_{eq}$ are trajectory-generating critical points of $\boldsymbol{f}$ with an unstable slowest eigenspace, such that $\partial\mathcal{M}_1^s$ is the set of at most two zero-dimensional critical solutions $\boldsymbol{z}_{eq}$ of $\boldsymbol{f}$ that satisfy criterion (2.35). Furthermore, $\mathcal{F}'$ is the flow originating from $\boldsymbol{z}_{eq} \in \partial\mathcal{M}_1^s$ perturbed along their slowest direction forward in time, i.e.

$$\mathcal{F}'(\boldsymbol{z}_{eq}, t) = \mathcal{F}(\boldsymbol{z}_{eq} + \epsilon\, \mathbf{v}_{s,eq}, t),\ \ \epsilon << 1,\ \ t \geq 0 \tag{2.40}$$

Equation (2.39) provides a constructive definition of the 1D SIM and is based upon its geometrical properties.

2.3.2.2 Hyperbolic Critical Points: Finite and Infinite Equilibria

By the above geometrical properties, it is evident that the critical points of the reduced source term $\boldsymbol{f}(\boldsymbol{z})$ are key to the construction of the SIM. A finite critical point $\boldsymbol{z}_{eq}$ of reactive system (2.28) is that for which

$$\boldsymbol{f}(\boldsymbol{z}_{eq}) = \boldsymbol{0}. \tag{2.41}$$

Furthermore, $\boldsymbol{z}_{eq}$ is hyperbolic if none of the eigenvalues of $\boldsymbol{f}_{\boldsymbol{z}}(\boldsymbol{z}_{eq})$, i.e. (2.33), have zero real part. These finite hyperbolic critical points can be classified according to the eigenspectrum of $\boldsymbol{f}_{\boldsymbol{z}}(\boldsymbol{z}_{eq})$ as follows. If all of the eigenvalues in (2.33) are real and negative, then $\boldsymbol{z}_{eq}$ is said to be a *sink*. It is, thus, a stable zero-dimensional manifold. If all of the eigenvalues in σ_2 are real and positive, then $\boldsymbol{z}_{eq}$ is said to be a *source*. Therefore, it is an unstable zero-dimensional manifold. Finally, if at least one eigenvalue in σ_2 is real and positive and another is real and negative, $\boldsymbol{z}_{eq}$ is said to be a *saddle*. There is an unstable manifold emmanating from a saddle, as well as a stable manifold converging into this type equilibrium point. It is immediately evident that $\partial\mathcal{M}_1^s$ is the set of at most two saddles that satisfy criterion (2.35). Note then that by the slowness property of the 1D SIM, its branches stem from saddles.

As shown in [46], (2.29) also has critical points at infinity. These are accessible by a compactification of phase space, which can be achieved by applying several different methods. A popular method is Poincare's sphere method, by which the phase

space is mapped onto a unit sphere. This yields an understandable and graphic representation of phase space, but it is not unique [46]. Another popular technique is the projective space method, through which infinite equilibria are found by a change of variables. The projective space method results in a new polynomial system, which is solved for its finite equilibria. These points are precisely the reduced source term's infinite equilibria. This method is brefiely described in the remainder of this section. For more detail on the derivation, advantages and disadvantages of this technique, the reader is referred to [47].

The projective space method consists of a simple transformation of the state variables $\boldsymbol{z}$ such that the polynomial system is mapped onto a different problem. To start with, a new set of variables is found by:

$$\begin{aligned} y_k &= \frac{1}{z_k},\ k \in \{1, 2, ..., n_s - n_e\} \\ y_i &= \frac{z_i}{z_k},\ i \neq k \end{aligned} \tag{2.42}$$

such that $\boldsymbol{y} \in \mathbf{Y} \subset \mathbb{R}^{n_s - n_e}$, where z_k is arbitrarily selected. The above equations map infinite equilibria upon the line $y_k = 0$ [47]. Next, it is important to identify the original polynomial system's maximum degree as d. Finally, by substituting the above into (2.28), a new polynomial system is obtained:

$$\boldsymbol{g}(\boldsymbol{y}) = y_k^d \begin{pmatrix} f_1(y_1, \ldots, y_{n_s-n_e}) - y_1 f_k(y_1, \ldots, y_{n_s-n_e}) \\ \vdots \\ -y_k f_k(y_1, \ldots, y_{n_s-n_e}) \\ \vdots \\ f_{n_s-n_e}(y_1, \ldots, y_{n_s-n_e}) - y_{n_s-n_e} f_k(y_1, \ldots, y_{n_s-n_e}) \end{pmatrix}. \tag{2.43}$$

Note that the Hartman-Grobman theorem also holds for a dynamical system

$$\frac{d\boldsymbol{y}}{dt} = \boldsymbol{g}(\boldsymbol{y}) \tag{2.44}$$

such that the critical points of $\boldsymbol{g}(\boldsymbol{y})$ can be classified according to the eigevalues of $\boldsymbol{g}_{\boldsymbol{y}}(\boldsymbol{y}_{eq})$. Furthermore, all finite critical points of $\boldsymbol{g}$ maintain their dynamical character when mapped back to $\boldsymbol{\Xi}$, i.e. a finite saddle of $\boldsymbol{g}$ is an infinite saddle of $\boldsymbol{f}$ and so on.

2.3.3 Intrinsic Low-Dimensional Manifold

The ILDM method proposed by Maas and Pope [1] is one of the many reduction techniques based on the slow-fast decomposition of system dynamics, along with computational singular perturbation (CSP) method [30] and flamelet-generated manifolds (FGM) method [48], amongst others. This popular method attempts to find the invariant attractor in phase space by decoupling fast and slow dynamics. It is by a suitable change of basis that the problem at hand is recast into a singular perturbation form and the two distinct motions are segregated [35, 40]. The fast modes, assumed extinct, are then solved as functions of a few slow progress variables $\boldsymbol{z}_\theta$, which parametrize the manifold for subsequent storage and retrieval. The parametrized manifold has an inherent error however, and as such it is not invariant. Thus the intrinsic low-dimensional manifold is only an approximation to the SIM. The approximation error is a function of the problem's spectral gap and the SIM's curvature [49].

The eigenspectrum (2.33) of the jacobian matrix $\boldsymbol{f_z}$ can be partitioned into slow and fast sets σ_s and σ_f provided that there exists a spectral gap $\varepsilon << 1$, i.e. the fastest eigenvalue in σ_s is still significantly smaller that the slowest eigenvalue in σ_f. With this at hand, consider the invariant decomposition of $\boldsymbol{f_z}$:

$$\boldsymbol{f_z} = \begin{pmatrix} \boldsymbol{Z}_s & \boldsymbol{Z}_f \end{pmatrix} \begin{pmatrix} \boldsymbol{T}_s & \boldsymbol{0} \\ \boldsymbol{0} & \boldsymbol{T}_f \end{pmatrix} \begin{pmatrix} \tilde{\boldsymbol{Z}}_s \\ \tilde{\boldsymbol{Z}}_f \end{pmatrix} \tag{2.45}$$

where the matrices $\boldsymbol{Z}$ and $\tilde{\boldsymbol{Z}}$ span the right and left invariant subspaces of the jacobian $\boldsymbol{f_z}$, such that

$$\tilde{\boldsymbol{Z}} = \boldsymbol{Z}^{-1}. \tag{2.46}$$

The $(n_s - n_e) \times m_s$ partition $\boldsymbol{Z}_s$ spans the m_s-dimensional slowest eigenspace $E^s_{m_s}$. Similarly, the $(n_s - n_e) \times m_f$ block $\boldsymbol{Z}_f$ spans the m_f-dimensional fast eigenspace $E^f_{m_f}$. Hence, these spaces previously introduced in section 2.3.2 can be redefined as:

$$\begin{aligned} E^s_{m_s} &= \text{span}(\boldsymbol{Z}_s) \\ E^f_{m_f} &= \text{span}(\boldsymbol{Z}_f) \end{aligned} \tag{2.47}$$

but could well be represented by an equivalent basis such as the orthogonal Schur vectors, or the eigenvectors of $\boldsymbol{f_z}$ themselves. The square matrices $\boldsymbol{T}_s$ and $\boldsymbol{T}_f$ are quasi-upper-triangular matrices with the real parts of the m_s slowest eigenvalues

$$\lambda_{i,s} \in \sigma_s,\ i = 1, \ldots, m_s \tag{2.48}$$

and m_f fastest eigenvalues in their diagonals

$$\lambda_{j,f} \in \sigma_f,\ j = m_s + 1, \ldots, m_s + m_f \tag{2.49}$$

respectively. Since fast modes are assumed extinct and slow modes govern the system's dynamics, the m_s-dimensional ILDM is given by:

$$\tilde{\boldsymbol{Z}}_f \boldsymbol{f}(\boldsymbol{z}) = \boldsymbol{0}. \tag{2.50}$$

By the above, the source term vector $\boldsymbol{f}(\boldsymbol{z})$ lies entirely on the m_s-dimensional slowest eigenspace, i.e.

$$\boldsymbol{f}(\boldsymbol{z}) \in E^s_{m_s}. \tag{2.51}$$

For nonlinear systems, the slowest eigenspace is not aligned with the tangent space $\boldsymbol{T}^{\mathcal{M}}$ of the manifold, as illustrated in fig. 2.5. The ILDM is not an invariant attractor in the affine subspace and hence the inherent error between the SIM and the ILDM.

System (2.50) provides a constructive definition of the ILDM, i.e.

$$\mathcal{M}^{ILDM} = \{\boldsymbol{z} \mid \tilde{\boldsymbol{Z}}_f \boldsymbol{f}(\boldsymbol{z}) = \boldsymbol{0}, \boldsymbol{z} \in \boldsymbol{\Xi}^+\}. \tag{2.52}$$

It is however numerically challenging to solve for the ILDM because (2.50) is a highly nonlinear underdetermined system of equations. This has motivated numerous works on the efficient calculation [41], refinement [34] and practical implementation [19] of the ILDM. Further works concerning the ILDM's numerical peculiarities regard parallelization and dynamic dimension reduction [50], adaptive tabulation strategies and coupling of transport processes [51] and reaction-diffusion extensions [52].

Finally, note that the above definitions could be formulated in composition space $\boldsymbol{\Psi}$ for system (2.11) without loss of generality. It is in the method's implementation that constructing the ILDM in reduced phase space $\boldsymbol{\Xi}$ becomes advantageous,

since σ_s will be rid of all zero eigenvalues related to conserved quantities.

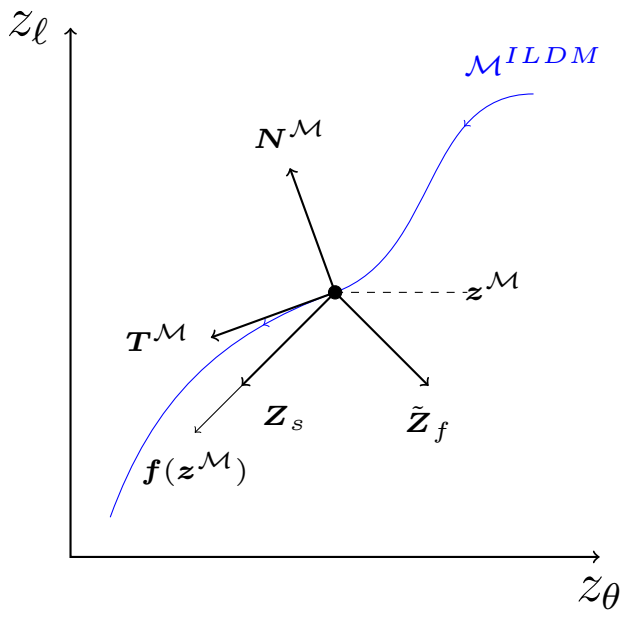

Figure 2.5: Geometrical picture of the ILDM $\mathcal{M}^{ILDM}$. Adapted from ref. [2] and ref. [3].

CHAPTER 3

NUMERICAL IMPLEMENTATION

The efficient calculation and refinement of reduced descriptions of chemicals kinetics has come to stand as a branch of computational fluid dynamics by itself. Amongst the different available techniques and algorithms, three common requirements are identified: the system's linear dependencies, the reaction operating conditions and rate coefficients correct evaluation. This chapter presents how to build upon this essential problem information to numerically solve for the slow invariant and intrinsic low-dimensional manifolds.

Gas discharge kinetics is challenging because transport and rate coefficients of free electrons derive from the electron energy distribution function. BOLSIG+ *is used to solve for and parametrize these coefficients, which are validated in a physical discharge simulation by a variable-order implicit ODE solver. Then, a particularly simple method from the literature for finding the 1D SIM is synthesized. Its implementation crosses several computational tools, but can be successfully carried out in a single one for moderate-size systems. Finally, the celebrated ILDM method and its implementation details are given.*

3.1 Reaction Rate Coefficients and Glow-Mode Non-Equilibrium Gas Discharge Validation

The physical reactive system (2.11) is stiff because of the presence of timescales that differ by several orders of magnitude. For computational efficiency a solver that can handle stiff problems is desired. There are several available routines with this capability, including MATLAB's `ode15s` and Octave's `LSODE`. SUNDIAL's `CVODE` was chosen to perform the integration of the system because of its powerful implicit methods and the fact that it is implemented within the adaptive mesh refinement (AMR) plasma-flow solver described in [18]. `CVODE` implicitly integrates stiff systems using backward-differencing formulae (BDF) of up to fifth order accuracy combined with Newton iterations. It solves the resulting linear system by direct methods, although Krylov methods are available and readily applicable for large stiff systems, where direct methods are unfeasible.

When the physical system (2.11) is discretized by variable order BDF, the resulting scheme reads:

$$\boldsymbol{G}(\boldsymbol{\psi}_n) = \sum_{i=0}^{K} \alpha_{i,n} \boldsymbol{\psi}_{n-i} + h_n \beta_n \boldsymbol{F}(\boldsymbol{\psi}_n) = \boldsymbol{0}, \tag{3.1}$$

where $\alpha_{0,n} = -1$, K is the integration order and h is the integration step size. All coefficients are determined by the solver structure and the recent history of step sizes. The m^{th} Newton iteration is thus given by:

$$[\boldsymbol{I} - h_n \beta_n \boldsymbol{F}_{\boldsymbol{\psi}}(\boldsymbol{\psi}_n^m)]\boldsymbol{\Delta}_n^m = \boldsymbol{G}(\boldsymbol{\psi}_n^m) \tag{3.2}$$

which, along with an initial guess based on data from previous iterations, yields the next iteration level state

$$\boldsymbol{\psi}_n^{m+1} = \boldsymbol{\psi}_n^m + \boldsymbol{\Delta}_n^m. \tag{3.3}$$

Convergence is achieved when

$$R \parallel \boldsymbol{\psi}_n^{m+1} - \boldsymbol{\psi}_n^m \parallel < \ 0.1\epsilon \tag{3.4}$$

where R is a convergence rate constant and $\| \cdot \|$ is the weighted root-mean-square norm. The weights are based on the user-provided absolute and relative tolerances. A maximum of three Newton iterations is permitted, although this can be adjusted [53]. The solver's structure is preset so that the linear system is solved with a direct dense method. As such, the first matrix of the left-hand side of (3.2) is never updated throughout an iteration. This choice is rooted in the fact that the models under analysis are of moderate size, but if a substantially larger system was to be studied, a Krylov method could readily substitute the current configuration.

The `CVODE`-based solver was implemented within a C++ *physics* class [54], which formally defines the system, its inputs, outputs and its solution. This class can in turn be incorporated to the aforementioned AMR plasma-flow solver. The physics class is also suited for reduction techniques as it incorporates LAPACK routines [55] that allow for slow-fast decomposition of $\boldsymbol{f}_z$, singular value decomposition of $\boldsymbol{\nu}$, and other relevant operations.

The plasma physics class contains a routine that evaluates the reaction rate coefficients for each discharge mechanism considered. Electron rate and transport parameters depend on electron energy distribution function (EEDF), i.e. the isotropic

term in the velocity distribution function of electrons. It generally is non-Maxwellian [29]. As such, the Boltzmann equation for electrons (BEE) must be solved for a given range of reduced electric fields. BOLSIG+ [56] is a BEE solver that provides steady-state solutions under the presence of uniform electric fields and outputs rate and transport coefficients, amongst other capabilities. Its only input is a set of collision cross-sections, promptly available in various databases. For the two gases considered in this study, the cross-sections were retrieved from the Phelps database [57,58] through the LXcat website [59]. The reaction rate coefficients are fitted assuming that the mean electron energy is in local equilibrium with the reduced electric field. Thus, the rate coefficient is given by a sixth-order polynomial of the electron temperature:

$$k_{r,e} = \exp\left[\sum_{i=0}^{6}\left(\frac{a_i}{{T_e}^i}\right)\right] \tag{3.5}$$

where T_e is the electron temperature in eV. The reduced mobility of electrons is fitted by:

$$\mu_e N_g = \exp\left[\sum_{i=0}^{8} b_i \ln^i(T_e)\right] \tag{3.6}$$

Fitting against mean energy is a well-established practice [60] which gives acceptable results in continuum plasma modeling, although BOLSIG+ itself provides fits for the rate coefficients as functions of the reduced field. Figures 3.1, 3.2, 3.3 and 3.4 show the polynomial fits for reaction rates and reduced mobility for discharges in Ar and N_2. Furthermore, fig. 3.5 shows mean electron energy against electric field for discharges in both background gases. Note that electrons are more energetic in Ar than they are in N_2. All BOLSIG+ runs were configured so that electron-electron collisions were considered for ionization degrees $N_e/N \geq 10^{-3}$, i.e. weakly ionized plasmas.

Simulation results are presented along with the aforementioned BOLSIG+ data in figures 3.6,3.7,3.9, while operating conditions for these benchmark cases are given in table 3.1. The systems ignite and reach equilibrium after a short transient, where production processes (e.g. ionization, excitation) are balanced by loss processes (e.g. recombination, de-excitation). The simplest Ar system perfectly exemplifies neutrality in a plasma column. Positive ion and electron concentrations are equal and considerably smaller than neutral concentration. The N_2 system requires a significantly higher reduced electric field to ignite, but achieves similar electron concentration and ionization fraction.

Table 3.1: Operating conditions for benchmark simulation cases.

Background Gas	P [kPa]	T_g [K]	V [V]	L [mm]
Ar	75	300	500	1
N_2	50	300	1000	1

The mechanisms of N_2 and Ar are presented in appendix A. The Ar discharge mechanism consists of three reaction clusters, through which reactions and species are added to itensify the complexity of the discharge. The first cluster is a basic ionization-recombination mechanism with neutrals, ions and electrons. The second cluster adds excitation reactions and metastables, while the third cluster adds bimolecular Ar ions.

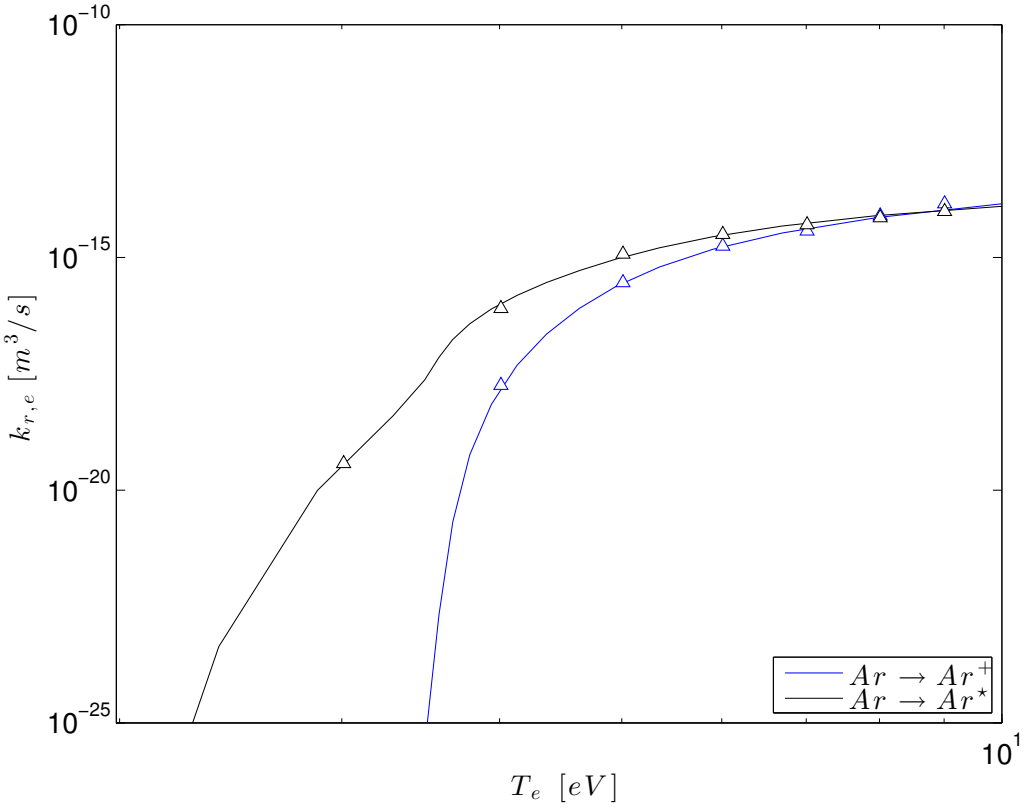

Figure 3.1: Electron collision reaction rate coefficients of a Ar discharge. The solid lines correspond to BOLSIG+ values while the markers correspond to the polynomial fits evaluated at certain electron temperatures.

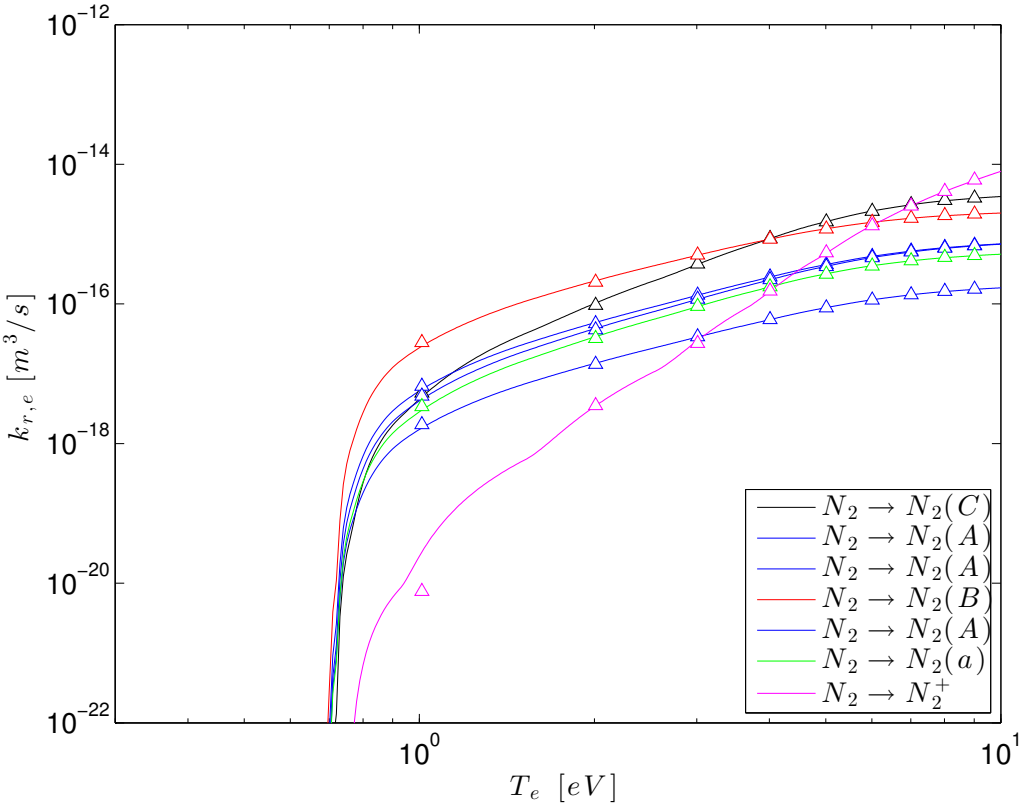

Figure 3.2: Electron collision reaction rate coefficients of a N_2 discharge. The solid lines correspond to BOLSIG+ values while the markers correspond to the polynomial fits evaluated at certain electron temperatures.

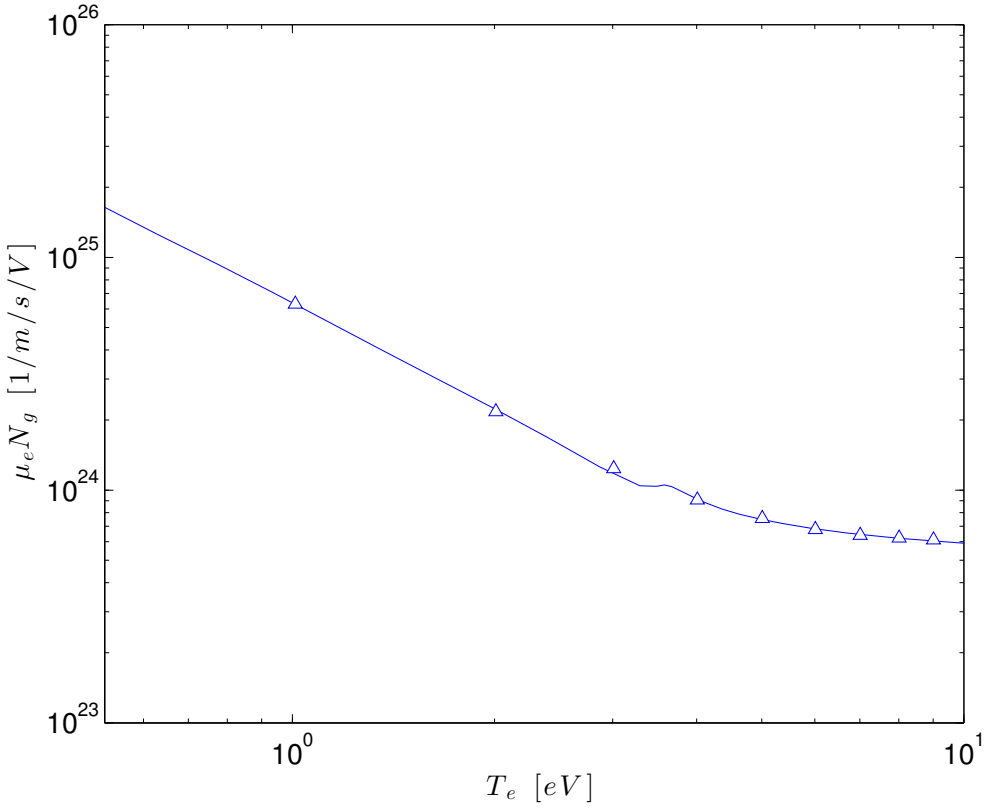

Figure 3.3: Electron reduced mobility in Ar. The solid lines correspond to BOLSIG+ values while the markers correspond to the polynomial fits evaluated at certain electron temperatures.

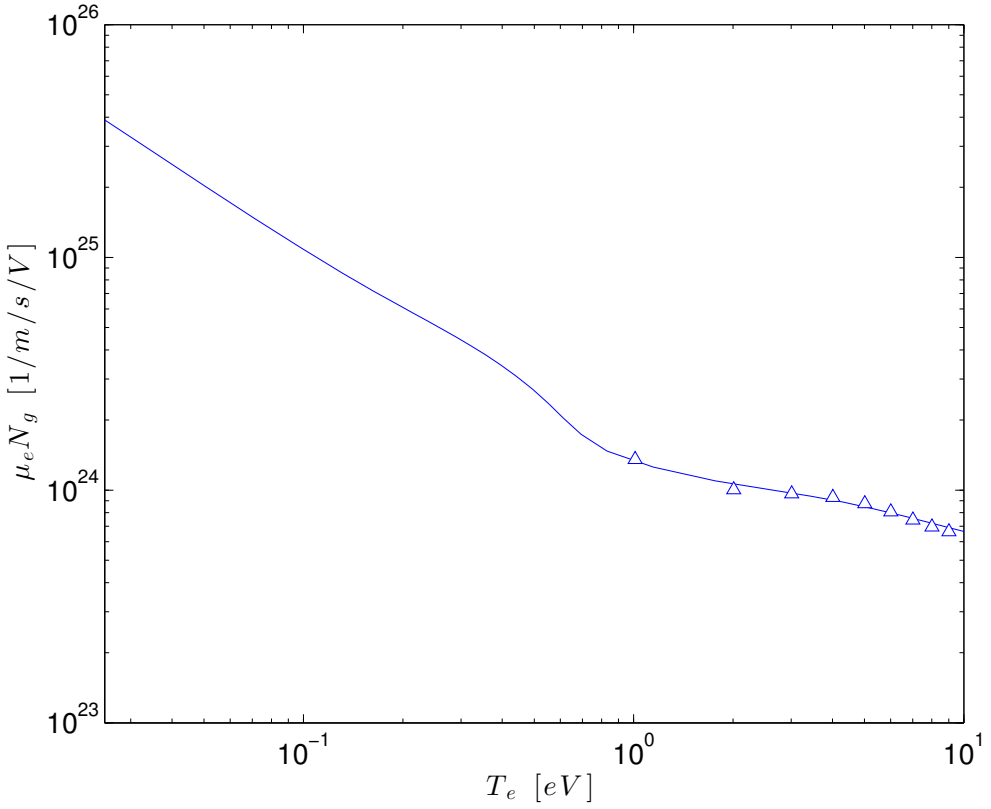

Figure 3.4: Electron reduced mobility in N_2. The solid lines correspond to BOLSIG+ values while the markers correspond to the polynomial fits evaluated at certain electron temperatures.

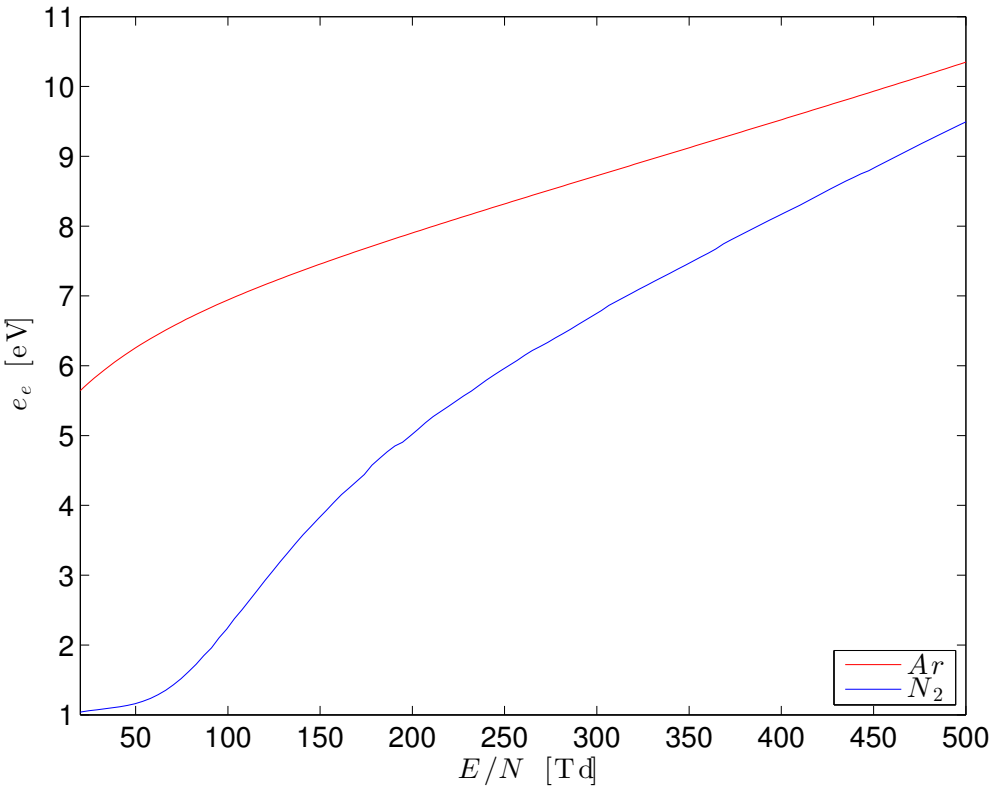

Figure 3.5: Electron mean energy ($e_e = 3\,T_e/2$) against reduced electric field for discharges in different backgroung gases Ar and N_2. Coefficients are fitted assuming e_e is in local equilibrium with E/N.

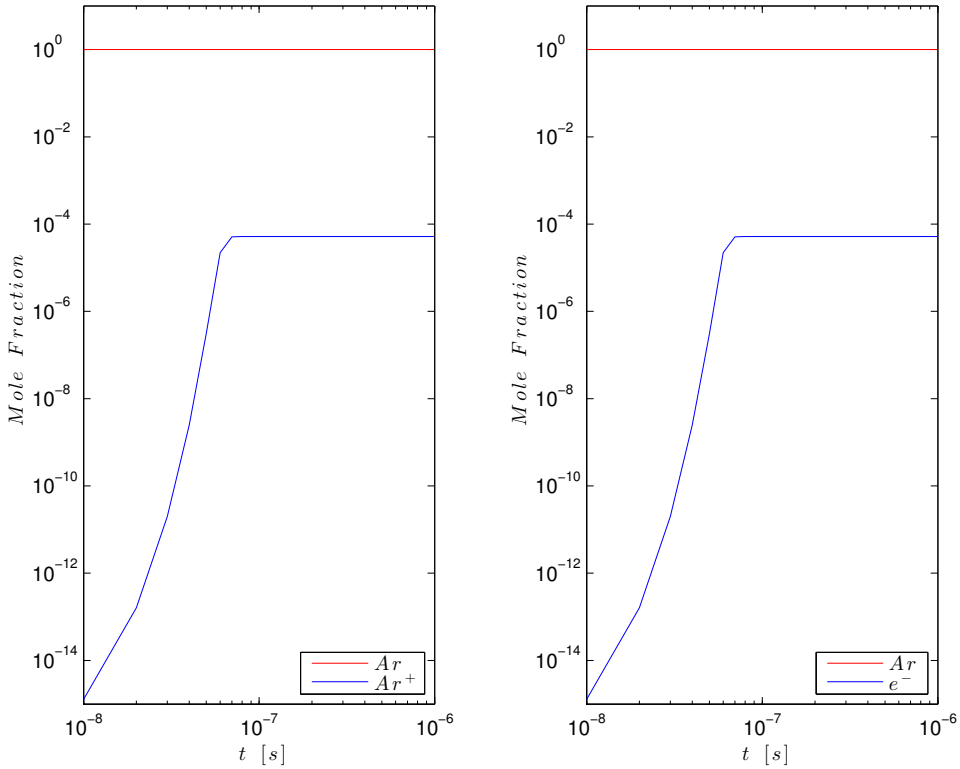

Figure 3.6: Discharge in Ar for $E/N = 27.13$ Td. The reaction mechanism is cluster 1 in table A.1.

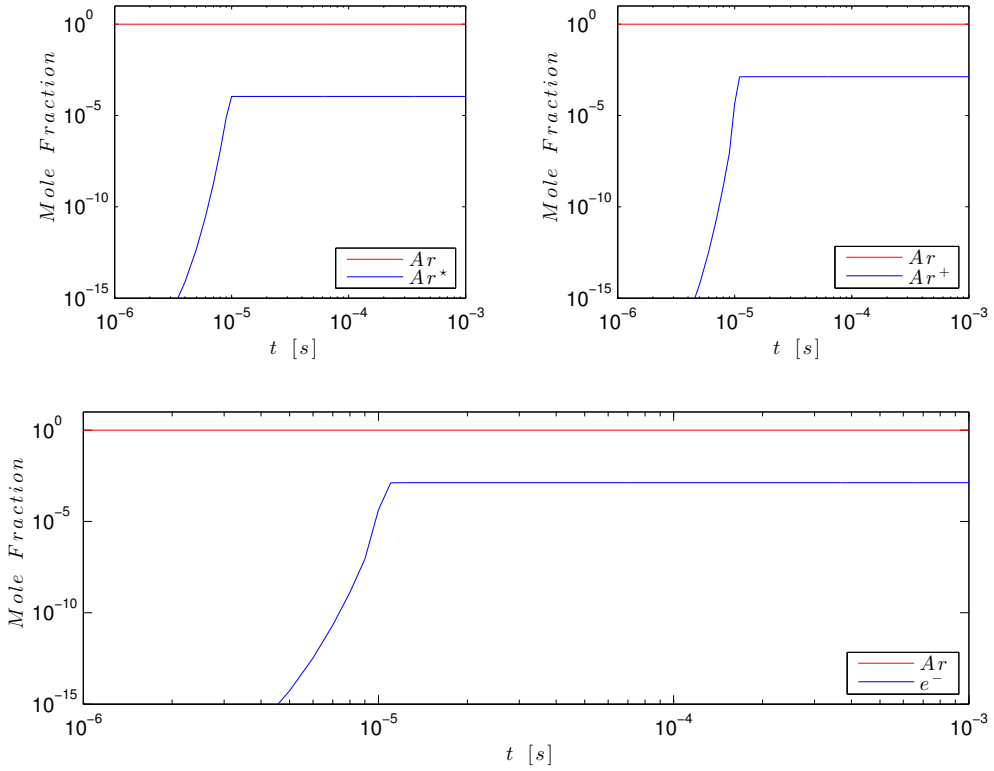

Figure 3.7: Discharge in Ar for $E/N = 27.13$ Td. The reaction mechanism are clusters 1 and 2 in table A.1.

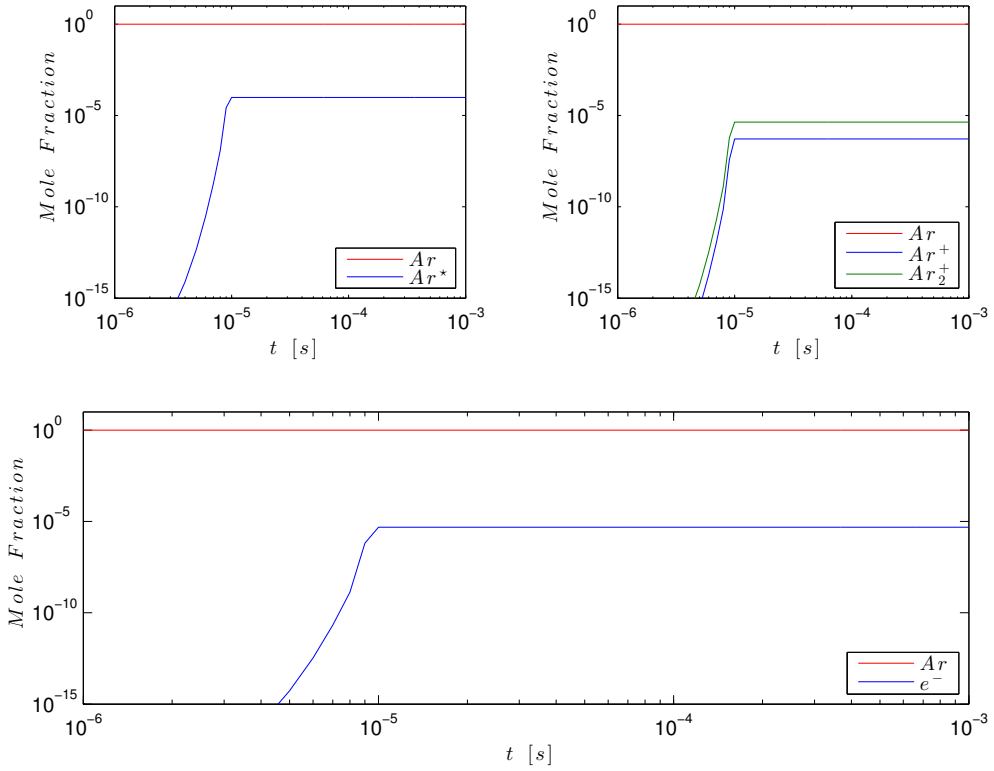

Figure 3.8: Discharge in Ar for $E/N = 27.13$ Td. The reaction mechanism are clusters 1, 2 and 3 in table A.1.

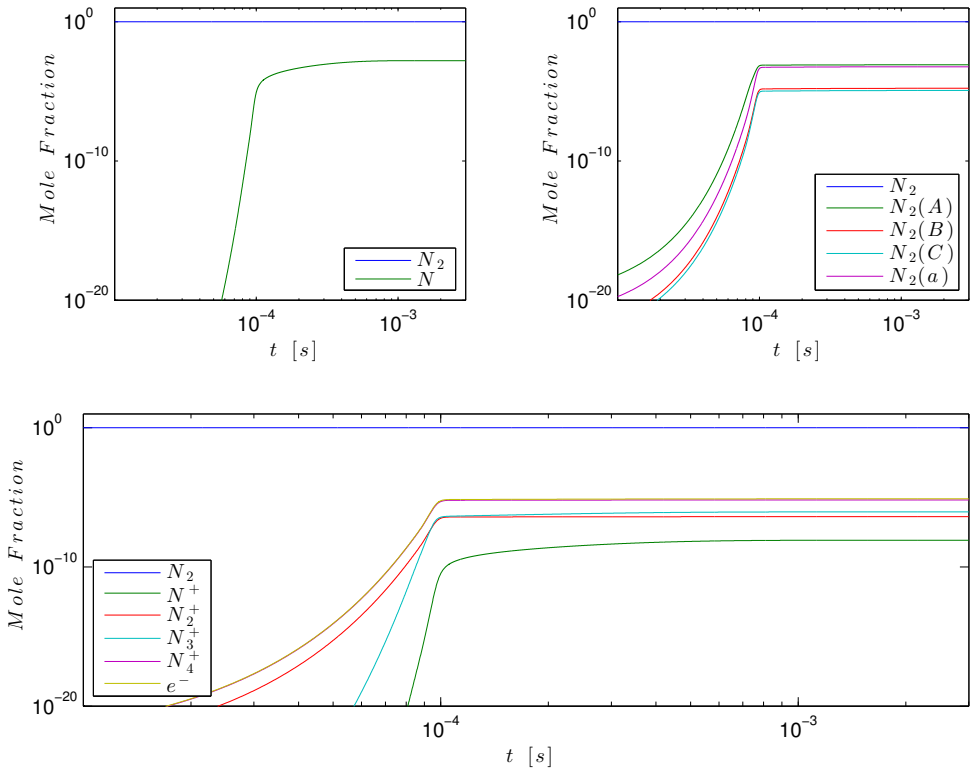

Figure 3.9: Discharge in N_2 for $E/N = 82.84$ Td. The reaction mechanism is given in table A.2.

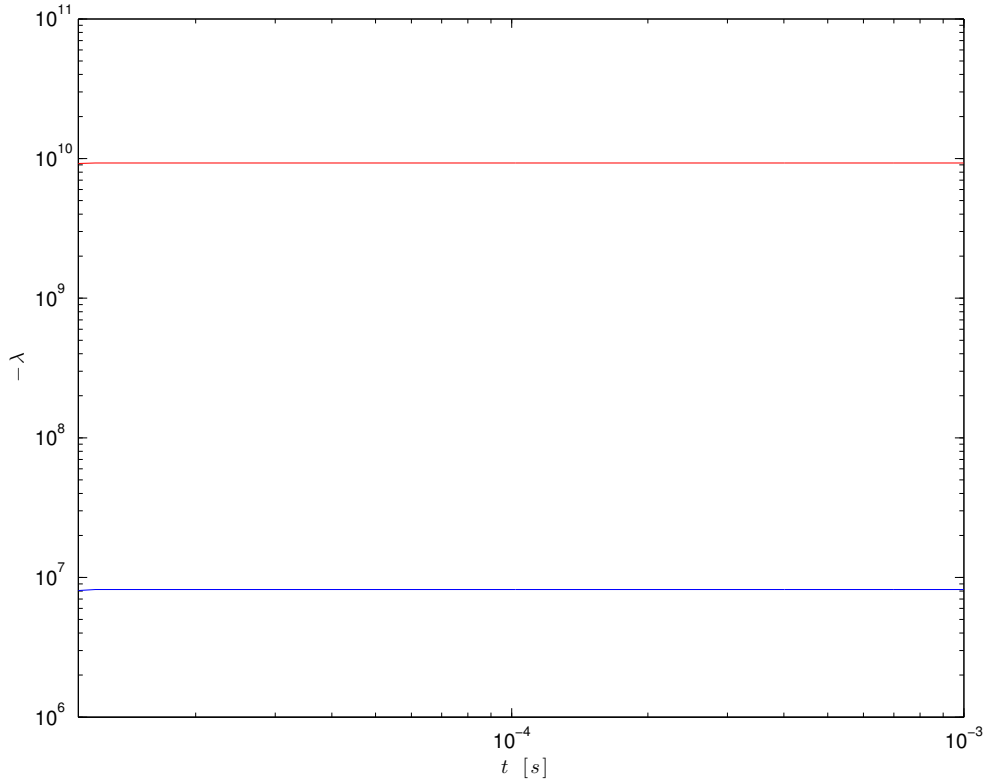

Figure 3.10: Evolution of the eigenspectra of the physical jacobian in a Ar discharge at $E/N = 27.13$ Td. A spectral gap always exists.

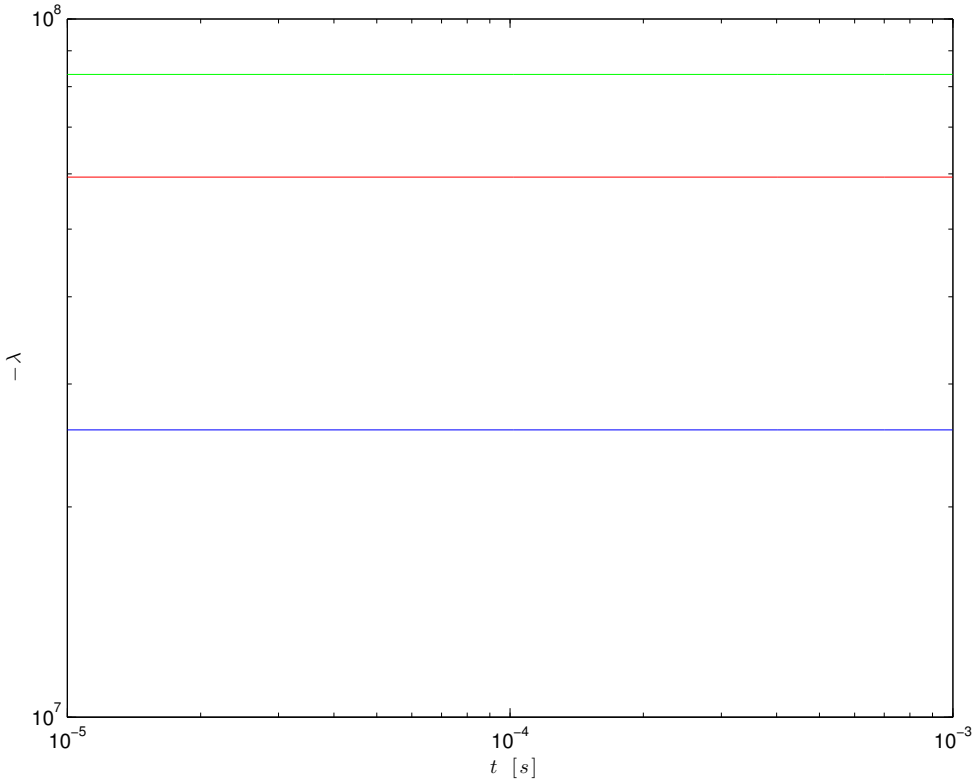

Figure 3.11: Evolution of the eigenspectra of the physical jacobian in a Ar discharge at $E/N = 27.13$ Td. A spectral gap always exists.

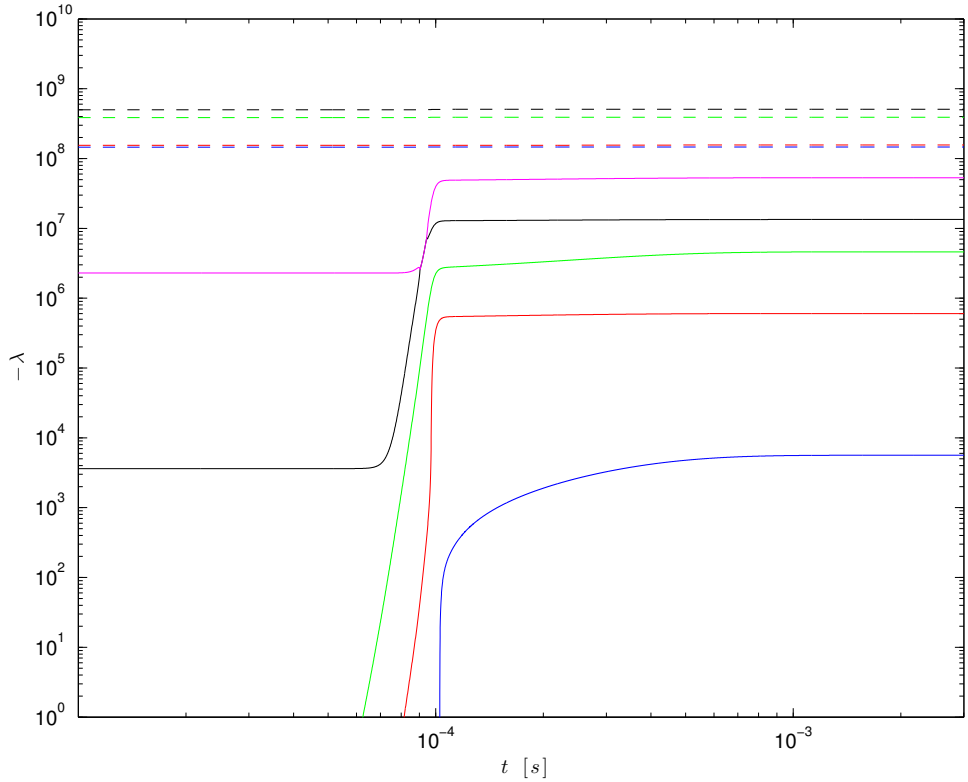

Figure 3.12: Evolution of the eigenspectra of the physical jacobian in a N_2 discharge at $E/N = 82.84$ Td. A spectral gap always exists.

3.2 One-Dimensional Slow Invariant Manifold Method

The method reported hereafter was introduced in ref. [37] and exploits the geometrical properties of the SIM by forward propagation of slow trajectories from saddle equilibria. It has been recognized for its simplicity and effectiveness, and all of its stages fall within two categories: identifying the systems equilibria and connecting slow trajectories.

Since the 1D SIM consists of at most two branches, it suffices to generate two heteroclinic orbits that asymptotically converge to physical equilibrium. Recall that these orbits are to stem from saddles, which are specific roots of the reduced system's source term. At this point, there is enough information about the 1D SIM to synthesize an elementary procedure for efficiently constructing it. This procedure consists of four different stages that can span different computational platforms or can be carried out alternatively with a single tool according to the system's dimensions.

The first stage, of analytical character, consists of constructing the reduced source term. The computational stage comes second, where all the isolated solutions of the reduced source term, finite and infinite, are found. These are classified or discarded according to the eigenvalues of the reduced jacobian matrix at each root in the processing stage. Finally, the reduced system is integrated along the slowest direction at each candidate saddle in the generation stage. If the emmanating branch converges to physical equilibrium, its attractiveness is evaluated. The procedure ends when two branches have been generated. The remainder of this section elaborates on each stage, its inputs, outputs and other implementation details.

To set up the problem accordingly in the analytical stage, it is important to note that both the physical (2.20) and reduced (2.29) source terms are polynomial systems of $\boldsymbol{\psi}$ and $\boldsymbol{z}$, respectively. These polynomial systems are determined by the physical system's linear dependecies $\boldsymbol{\nu}$, operating conditions and reaction rates only. *Mathematica*'s analytical capabilities can be exploited to build these polynomials following the constructive nature of section 2.2 as long as the above requirements are provided. However, these polynomials will be poorly scaled because of the sparse magnitudes of their coefficients, rendering any root finding algorithm inefficient. Once the reduced source term has been constructed, its polynomial structure is passed through MATLink to HomLab [61], a MATLAB library for solving moderate-size polynomial systems. HomLab will scale the polynomial and return two vectors $\boldsymbol{\alpha}$ and $\boldsymbol{\beta}$ of size $n_s - n_e$ such that:

$$\hat{f}_i(\hat{z}_i) = \alpha_i f_i(\beta_i z_i), \;\; i = 1, 2, ..., n_s - n_e \tag{3.7}$$

where $\hat{\boldsymbol{f}}(\hat{\boldsymbol{z}})$ is a new scaled polynomial system. This scaled system is the one that is actually solved for in the computational stage. To terminate the first stage, the size of the system must be pondered upon. *Mathematica*, like HomLab, can solve moderate-size systems such as those that model noble gas discharges, but underperforms with larger systems, such as those that model air and air-like mixtures discharges. If *Mathematica* is to solve for the roots of (3.7), then it proceeds to stage two. Otherwise, it generates an input file for a different software in the second stage.

The computational stage is preferably performed using a solver that offers the possibility of running on multicore computer architectures. Bertini [62] is a robust

homotopy continuation software for finding all the roots, zero-dimensional and multi-dimensional, of a polynomial system with such capability. It only requires an input script containing the polynomial system and will deliver several output files, amongst which only one containing the real finite solutions is of interest. For the present work, the software has been built on the TACC Stampede system.

The real finite solutions are exported into either *Mathematica* or MATLAB with the intention of finding the eigenspectrum of $\boldsymbol{f}_{\boldsymbol{z}}(\boldsymbol{z}_{eq})$ and classifying sources, sinks and saddles. Sources are immediately discarded. Only one sink is kept, which lies on physical space. Since the SIM is one-dimensional, only saddles with one unstable direction are kept. A further criterion imposed on saddles is that they immediately satisfy attractriveness (2.35). Note that the eigenspectrum is not obtained by the usual eigendecomposition, but rather by the Schur decomposition of $\boldsymbol{f}_{\boldsymbol{z}}(\boldsymbol{z}_{eq})$

$$\boldsymbol{f}_{\boldsymbol{z}}(\boldsymbol{z}_{eq}) = \mathbf{Q}\,\mathbf{T}\,\mathbf{Q}^{T}. \tag{3.8}$$

This is more convinient because the Schur vectors form an orthogonal basis. The eigenvalues appear in the diagonal of the Schur matrix $\mathbf{T}$ and are ordered by descending real part with a similarity transformation [63]. The slowest eigenspace of the system is spanned by the leftmost Schur vector of $\mathbf{Q}$.

Finally, the last stage consists of generating trajectories from candidate saddles. The reduced system (2.28) is numerically integrated for each of the n_{eq} candidate saddles with initial condition

$$\boldsymbol{z}(\mathbf{0}) = \boldsymbol{z}_{eq,i} + \epsilon\,\mathbf{q}_s, \;\; \epsilon << 1, \;\; i = 1, 2, ..., n_{eq} \tag{3.9}$$

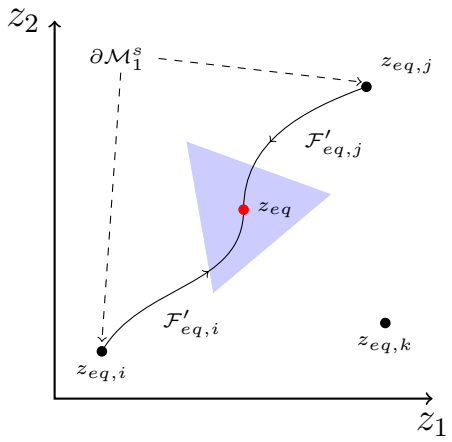

Figure 3.13: Typical structure of the 1D SIM. Trajectories are generated from saddles with an unstable one-dimensional slowest eigenspace.

i.e. the system is slightly perturbed in the direction of its slowest Schur vector. This task can be carried out in a wide variety of frameworks. Since (2.28) retains the timescale structure of (2.11), an ODE solver suite that can handle stiff problems is required. SUNDIALS Implicit Differential-Algebraic (IDA) solver is implementable in *Mathematica* through `NDSolve`, allowing for a backward Euler scheme with Newton iterations, similar to the integration scheme of the physical system (2.11) in section 3.1. MATLAB's `ode15s` is also a good alternative in case the roots where found using Bertini. This procedure is looped until at most two trajectories have been found to converge to the only realizable sink of the system. Finally, their attractiveness is verified and the manifold is stored.

3.2.1 Validation

The procedure described above and the scripts generated according to it were validated against the Zel'dovich test case that appears in [37]. Consider the two-reversible-reactions Zel'dovich mechanism for nitric acid production given in table

3.2. The backward reaction rate $k_{b,r}$ of reaction r is a function of the equilibrium constant K_r, which in turn is a function of reaction temperature T. The former two are given by

$$k_{b,r} = \frac{k_{f,r}}{K_r} \tag{3.10a}$$

$$K_r = \exp\left(- \frac{\boldsymbol{\nu}_r \cdot \boldsymbol{G}^\circ}{R_u T} \right) \tag{3.10b}$$

where $k_{f,r}$ is the forward reaction rate, shown in table 3.2, ν_r is the r^{th} vector in the reaction matrix $\boldsymbol{\nu}$ and $\boldsymbol{G}^\circ$ is the vector of the involved species' standard Gibbs free energies at reaction temperature T. This vector is created by using the Shomate equations

$$H_s^\circ - H_{s,f}^\circ = A\,\mathcal{T} + \frac{B}{2}\,\mathcal{T}^2 + \frac{C}{3}\,\mathcal{T}^3 + \frac{D}{4}\,\mathcal{T}^4 + E\,\mathcal{T}^{-1} + F - H \tag{3.11a}$$

$$S_s^\circ = A\ln(\mathcal{T}) + B\,\mathcal{T} + \frac{C}{2}\,\mathcal{T}^2 + \frac{D}{3}\,\mathcal{T}^3 - 2E\,\mathcal{T}^{-2} + G \tag{3.11b}$$

where $\mathcal{T} = T \times 10^{-3}$, H_s° and S_s° are the standard enthalpy and entropy of species s, in kJ/mol and J/mol $- K$, respectively, $H_{s,f}^\circ$ is the enthalpy of formation of species species s, in kJ/mol, and by definition

$$G_s^\circ = H_s^\circ - T\,S_s^\circ \tag{3.12}$$

The Shomate coefficients were retrieved from the NIST reference database no. 69 [64]. In the case where the curvefits were not available through this database, the JANAF tables were used [65].

This is enough to set up the problem. Note that, even though $n_s = 5$ and $n_e = 2$, there is a further constraint, namely that all reactions are bimolecular, and

Table 3.2: Zel'dovich mechanism for nitric acid formation, intended for 1D SIM method validation. Reaction rate coefficients are given in units of $\mathrm{cm}^3/\mathrm{mol}-\mathrm{s}$.

No.	Reaction	Forward Rate Coefficient	Ref.
(1)	$N + O_2 \rightleftharpoons NO + O$	$5.841 \times 10^9 T^{1.01} \exp(\frac{-6195.6}{R_u T})$	[37]
(2)	$N + NO \rightleftharpoons N_2 + O$	21.077×10^{12}	[37]

as such the reduced phase space $\boldsymbol{\Xi}$ is two-dimensional. The manifold was found for a reaction temperature of 4000 K and a volume of 10^3 cm^3. The reduced source term contains several roots both finite and infinite, but only three are relevant to the construction of the manifold. These are shown in table 3.3. Of all the roots, shown or not, only R_1 lies within the physically realizable region and thus is the system's physical equilibrium. The manifold, depicted in fig. 3.15, consists two branches, one stemming from a finite saddle R_2 and another stemming from an infinite saddle I_1. This last point is nonhyperbolic, and as such, the Hartman-Grobman theorem cannot be used to analyze its dynamical character. For more details on this peculiarity, the reader is referred to ref. [37].

Table 3.3: Relevant roots of the Zel'dovich mechanism reduced source term. R_1 and R_2 are finite points, while I_1 is a root at infinity.

Root	(z_1, z_2) or (y_1, y_2)	(λ_s, λ_f)	Type
R_1	$(3.042 \times 10^{-3}, 2.943 \times 10^{-5})$	$(-2.387 \times 10^5, -2.509 \times 10^7)$	Sink
R_2	$(-4.185 \times 10^{-3}, -2.663 \times 10^{-5})$	$(3.700 \times 10^5, -1.613 \times 10^7)$	Saddle
I_1	$(0, 0)$	$(0, -1.275 \times 10^9)$	Saddle

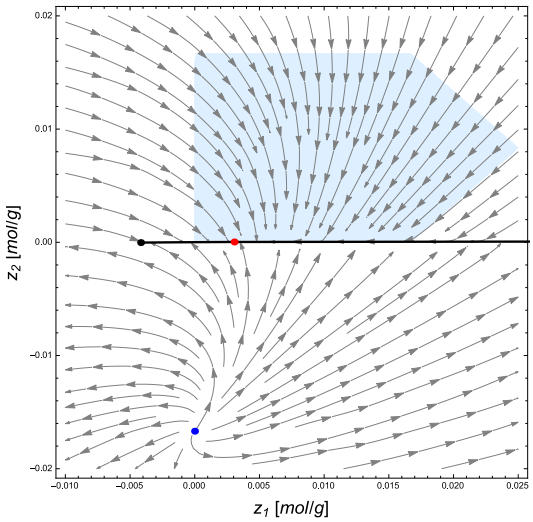

Figure 3.14: Spatially homogeneous 1D SIM for the system described by the Zel'dovich mechanism. The red marker corresponds to physical equilibrium, while black and blue markers correspond to finite saddles and sources, respectively. An irrelevant source is marked in blue. The light blue region is the physically realizable space, i.e. $\boldsymbol{\psi}(\boldsymbol{z}) \geq 0$.

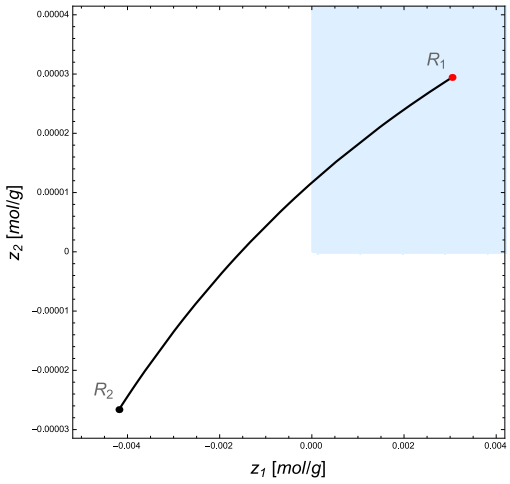

Figure 3.15: A closer look of the SIM's leftmost branch. Generated from saddle R_2, it converges to physical equilibrium R_1.

3.3 Intrinsic Low-Dimensional Manifolds Method

The ILDM equation is traditionally solved by predictor-corrector continuation methods. Originally, pathfollowing codes such as `PITCON` [66], supplemented with manifold boundary evaluation routines, were used to solve for and parametrize the ILDM [1]. Eventually, detailed procedures suited to the inherent characteristics of the problem were developed. The methodology presented in this section follows that proposed by Maas in [41].

The ILDM method described below has been implemented in both MATLAB and C++. The C++ version of the code relies on the *PlasmaPhysics* class created for discharge simulations. Furthermore, it is linked to the LAPACK library for all matrix operations. The algorithm starts at a point known to reside in the ILDM, such as physical equilibrium, and runs a predictor-corrector continuation process until it meets the system's boundaries determined by its constraints, i.e. mass possitivity and mole fraction unity. The first step consists of computing and partitioning the real Schur decomposition of the local jacobian $\boldsymbol{f}_{\boldsymbol{z}}$ at a point $\boldsymbol{z}_{\mathcal{M}}$ on the manifold

$$\boldsymbol{f}_{\boldsymbol{z}}(\boldsymbol{z}_{\mathcal{M}}) = \begin{pmatrix} \boldsymbol{Q}_s & \boldsymbol{Q}_f \end{pmatrix} \begin{pmatrix} \boldsymbol{T}_s & \boldsymbol{T}_{sf} \\ \boldsymbol{0} & \boldsymbol{T}_f \end{pmatrix} \begin{pmatrix} \boldsymbol{Q}_s^T \\ \boldsymbol{Q}_f^T \end{pmatrix} \tag{3.13}$$

rewritten here for clarity. The block sizes are determined by the user's desired ILDM dimension. The rest of the study however, concerns 1D manifolds. The above is obtained using LAPACK's `DGEES`, while `DTREXC` is iteratively used to sort the eigenvalues in descending order of their real parts along the diagonal of the quasi-

upper-triangular matrix $\mathbf{T}$ by an orthogonal similarity transformation [55]. The same routine solves the Sylvester equation

$$\boldsymbol{T}_s\boldsymbol{M} - \boldsymbol{M}\boldsymbol{T}_f = -\boldsymbol{T}_{sf} \tag{3.14}$$

using `DTRSYL` to construct the invariant decomposition (2.45), where the local right and left invariant subspaces are given by:

$$\tilde{\boldsymbol{Z}} = \begin{pmatrix} \boldsymbol{I} & -\boldsymbol{M} \\ \mathbf{0} & \boldsymbol{I} \end{pmatrix} \mathbf{Q}^T \tag{3.15a}$$

$$\boldsymbol{Z} = \mathbf{Q} \begin{pmatrix} \boldsymbol{I} & \boldsymbol{M} \\ \mathbf{0} & \boldsymbol{I} \end{pmatrix}. \tag{3.15b}$$

It is with the above, along with suitable a parametrization of the manifold, that the algorithm tracks the ILDM in phase space.

3.3.1 Manifold Parametrization

By providing a parametrization $\boldsymbol{P}(\boldsymbol{z})$ of the ILDM, the otherwise underdetermined system of equations (2.50) is complete. Furthermore, dimension reduction is succesfully achieved by representing all phase variables by a smaller set of parametrizing variables $\boldsymbol{z}_\theta$, also called reaction progress variables. The new parametrized system reads

$$\boldsymbol{G}(\boldsymbol{z}) = \begin{pmatrix} \tilde{\boldsymbol{Z}}_f \boldsymbol{f}(\boldsymbol{z}) \\ \boldsymbol{P}(\boldsymbol{z}) \end{pmatrix} = \mathbf{0}. \tag{3.16}$$

The parametrization function is significantly more complex if the ILDM were to be solved in composition space $\boldsymbol{\Psi}$ because it has to account for conserved scalars. Thus, it can be split into conservation parametrization and reaction progress functions

$$\boldsymbol{P} = \begin{pmatrix} \boldsymbol{P}^{\boldsymbol{\xi}} \\ \boldsymbol{P}^{\boldsymbol{\theta}} \end{pmatrix}. \tag{3.17}$$

Since this work deals with manifolds in reduced space $\boldsymbol{\Xi}$, there will be no further insight into $\boldsymbol{P}^{\boldsymbol{\xi}}$ and only the parametrization of progress variables will be pondered upon. This function indicates the direction in which the pathfollowing algorithm searches for a new point on the manifold. Note that there is no physical motivation for the parametrization, motivating a routine that updates it after every predictor-corrector step. This has not been implemented however, as a simpler parametrization algorithm was preferred. Thus, the parametrization of the manifold is:

$$\boldsymbol{P}^{\boldsymbol{\theta}}(\boldsymbol{z}) = P^{\boldsymbol{\theta}}_{\mathcal{M}}[\boldsymbol{z} - \boldsymbol{z}_{\mathcal{M}}] \tag{3.18}$$

where $P^{\boldsymbol{\theta}}_{\mathcal{M}}$ is a $m_s \times (n_s - n_e)$ matrix, which in this particular one-dimensional case, i.e. $m_s = 1$, is given by

$$P^{\boldsymbol{\theta}}_{\mathcal{M}} = \boldsymbol{e}_i^T \tag{3.19}$$

where $\boldsymbol{e}_i$ is the i^{th} unit vector such that $\boldsymbol{z}_\theta = \boldsymbol{z}_i$.

3.3.2 Continuation Procedure

The continuation process implemented as per ref. [41] is a predictor-corrector algorithm which tracks the manifold in a user-specified direction $\boldsymbol{\delta}$ with a user-

specified stepsize ζ. Since the objective is to track a one-dimensional manifold, the direction vector $\boldsymbol{\delta}$ is chosen to be a unit vector $\boldsymbol{e}_i$ to satisfy

$$P_{\mathcal{M}}^{\boldsymbol{\theta}} \boldsymbol{v}_p = \zeta \boldsymbol{\delta}. \tag{3.20}$$

The predictor step is based upon the fact that, by definition, the tangent subspace of the manifold is approximated by the slowest eigenspace, such that a predictor

$$\boldsymbol{v}_p = \zeta Z_s [P_{\mathcal{M}}^{\boldsymbol{\theta}} Z_s]^{-1} \boldsymbol{\delta} \tag{3.21}$$

yields a predicted point $\boldsymbol{z}_p$ in the following manner:

$$\boldsymbol{z}_p = \boldsymbol{z}_{\mathcal{M}} + \boldsymbol{v}_p. \tag{3.22}$$

The corrector step is a Newton solver for the augmented nonlinear system

$$\boldsymbol{H}(\boldsymbol{z}) = \begin{pmatrix} \tilde{\boldsymbol{Z}}_f \boldsymbol{f}(\boldsymbol{z}) \\ P_{\mathcal{M}}^{\boldsymbol{\theta}} [\boldsymbol{z} - \boldsymbol{z}_p] \end{pmatrix} = \boldsymbol{0} \tag{3.23}$$

with initial guess $\boldsymbol{z}^0 = \boldsymbol{z}_p$. The m^{th} general Newton iteration, given by:

$$\boldsymbol{H}_{\boldsymbol{z}}(\boldsymbol{z}^m) \boldsymbol{\Delta}^m = -\boldsymbol{H}(\boldsymbol{z}^m) \tag{3.24}$$

yields the next iterate

$$\boldsymbol{z}^{m+1} = \boldsymbol{z}^m + \boldsymbol{\Delta}^m \tag{3.25}$$

where the augmented system's jacobian matrix $\boldsymbol{H}_{\boldsymbol{z}}$ is approximated by:

$$\boldsymbol{H}_{\boldsymbol{z}} \approx \begin{pmatrix} \tilde{\boldsymbol{Z}}_f \boldsymbol{f}_{\boldsymbol{z}} \\ P^{\boldsymbol{\theta}}_{\mathcal{M}} \end{pmatrix}. \tag{3.26}$$

The corrector step was implemented using `NLEQ1`, a robust Newton solver for highly nonlinear problems. This procedure converges to a corrected point $\boldsymbol{z}_c$, which is then submitted to a boundary-check. If the value lies within physically realizable space, it is stored and a new overall ILDM iteration is carried on. Consequently, each ILDM iteration consists of a fast-slow decomposition, a parametrization step, a predictor-corrector step, a boundary check and a final storage phase. A simple MATLAB implementation of the ILDM method can be found in appedix B. It includes a routine for evaluation the reduced source term (2.29) and reduced jacobian (2.32) for the benchmark discharge in Ar modeled by reaction clusters 1 and 2 of table A.1.

3.3.3 Validation

The ILDM for the Zel'dovich mechanism was found in order to validate the method's implementation. Starting from physical equilibrium, denoted as R_1 in table 3.3, the predictor-corrector continuation procedure was carried out in two directions until each branch met the boundaries of the realizable region. The manifold is parametrized by $z_\theta = z_1$ and it closely approximates the 1D SIM. The manifold is shown in fig. 3.16

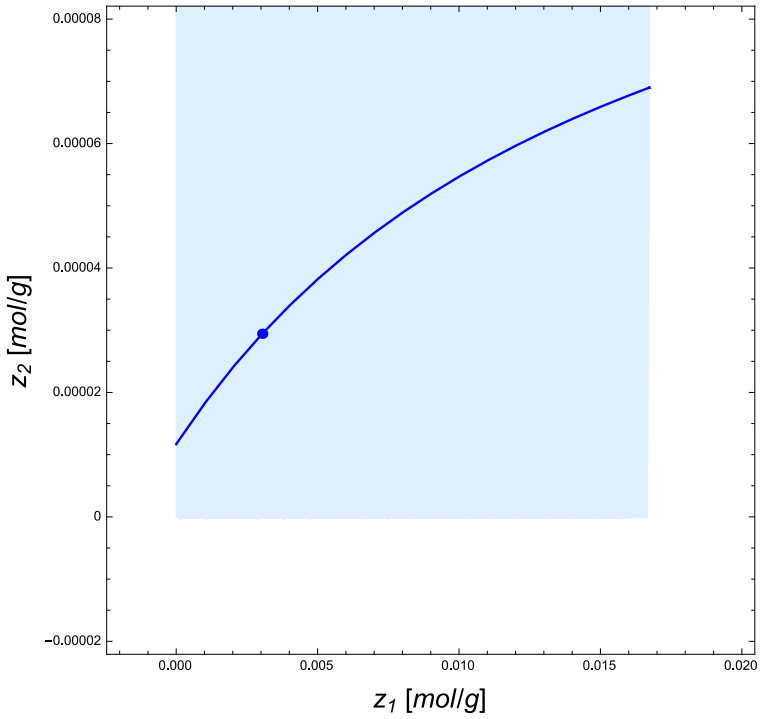

Figure 3.16: ILDM for the system described by the Zel'dovich mechanism. The blue marker corresponds to physical equilibrium

CHAPTER 4

REDUCED-ORDER MODELS OF GAS DISCHARGES

The 1D SIM and the ILDM may serve different purposes despite both being reduced-order models of chemical reaction dynamics. While the former brings insight into the structure and behavior of the slow motions in phase space, the latter is practical and readily implementable in large multi-dimensional CFD codes. These manifolds are thus potential tools to study the intrinsic complexities of gas discharges.

This chapter features the 1D SIM and ILDM, found with the previously exposed methods, of simple discharges in noble gases. The structure of the manifolds is briefly addressed and relevant critical points are tabulated. A bifurcation analysis of DC discharges in Ar is carried out to explain the system's behavior when subjected to an increasing electric field.

4.1 Slow Invariant Manifolds of Noble Gas Electrical Discharges

Consider the spatially homogeneous electrical discharge in Ar at benchmark operating conditions, given in table 3.1, and modeled by clusters 1 and 2 of table A.1. This is a $n_s = 4$, $n_e = 2$, $n_r = 6$ system, where mass and charge are conserved, so that the reduced subspace $\boldsymbol{\Xi}$ is two-dimensional. The physically realizable region is shown within $\boldsymbol{\Xi}$ in fig. 4.1 as a shaded polygon. The phase flow already suggests the existance of an attractor along the upper boundary of the physically realizable region.

The linear operator that transforms from physical to reduced space for this particular problem is:

$$\mathcal{D} = \begin{pmatrix} 0.7236 & 0.2764 \\ -0.2764 & -0.7236 \\ -0.4472 & 0.4472 \\ -0.4472 & 0.4472 \end{pmatrix}. \tag{4.1}$$

Thus, the reduced source term is a third-order polynomial system, which can be expressed as:

$$\boldsymbol{f}(\boldsymbol{z}) = \begin{pmatrix} \sum_{j=0}^{3} \sum_{i=0}^{3} a_{i,j}\ z_1^i\ z_2^j \\ \sum_{j=0}^{3} \sum_{i=0}^{3} b_{i,j}\ z_1^i\ z_2^j \end{pmatrix}. \tag{4.2}$$

Similarly, by applying the projective space method with $k = 1$, i.e.

$$y_1 = \frac{1}{z_1},\ \ y_2 = \frac{z_2}{z_1} \tag{4.3}$$

a new function, whose roots are the infinite equlibria of eq. (4.2), is formulated:

$$\boldsymbol{g}(\boldsymbol{y}) = \begin{pmatrix} \sum_{j=0}^{3} \sum_{i=0}^{3} c_{i,j}\ y_1^i\ y_2^j \\ \\ \sum_{j=0}^{3} \sum_{i=0}^{3} d_{i,j}\ y_1^i\ y_2^j \end{pmatrix}. \tag{4.4}$$

Recall that only saddles with one positive eigenvalue and physically realizable sinks are relevant to the 1D SIM's construction. These were found using *Mathematica* because of the system's moderate size. Finite roots, denoted as R_i, and all relevant infinite critical points, denoted as I_i are shown in table 4.1, along with the corresponding eigenvalues of the jacobian $\boldsymbol{f_z}$. R_1 is immediately identified as physical equilibrium, matching the value obtained with physical discharge simulations shown in fig. 3.7. Futhermore, R_2, R_3 and I_2 are all candidate generators. All of these points meet attractiveness criterion (2.35).

The first generated orbit stems from I_2 since it has the slowest of all corresponding eigenvalues. This orbit is successful, converging into physical equilibrium. Furthermore, it passes through R_3, such that it would be redundant to perturb the system from its slowest direction. The second branch is obtained by slightly perturbing the system from R_2. The manifold is shown in fig. 4.2, while its detailed structure can be found in fig. 4.3. By inspection, the submerged section of the lower branch corresponds to weak ionization, while the upper branch corresponds to higher ionized states. Thus, for problems such as DBD actuation, the lower branch would be of key interest. As for the upper branch, recombination must dominate this region because any deviation from equilibrium is immediately damped [18]. Another peculiarity of the manifold is that the high ionization branch not only behaves linearly,

but lies entirely in R_1's, and consequently R_2's, slowest eigenspace, as shown in fig. 4.4.

The existence of a high ionization SIM branch motivates a bifurcation analysis, whereby structural changes of the SIM are investigated under increasingly large electric fields. In other words, this analysis seeks to answer the following question: what happens to the SIM under severe electric fields? The same $n_s - n_e = 2$, $n_r = 6$ system was subjected to a wide range of reduced fields under the same background gas temperature $T_g = 300K$ and pressure $p_g = 75$kPa. The manifold shown in fig. 4.2 and 4.3 exists for a small range of low fields from 10 Td to 28 Td. This means that all R_1, R_2 and I_2 remain around the same location in phase space and their corresponding eigenspectra does not change qualitatively. This fact is interesting because this low range corresponds to moderate electron temperatures present in flow control applications. However, as the reduced electric field is increased, R_2 and I_2 remain fixed saddles in phase space but R_3 disappears and R_1 shifts along the higher ionization states towards R_2. Moreover, their corresponding eigenspectra begin to change quantitatively towards a qualitative change, i.e. a bifurcation. After a threshold reduced field, R_2 becomes a sink and R_1, which by then has shifted significantly along the high ionization states, becomes a saddle. The system's equlibrium point becomes unphysical, and it runs away. This behavior is analogous to that of explosion models in combustion previously reported [44] and can be observed in fig. 4.7 and 4.8.

Table 4.1: Relevant roots of the Ar discharge mechanism reduced source term at $E/N = 27.13$ Td. R_i are finite critical points $\boldsymbol{z}_{eq}$, while I_i are infinite critical points $\boldsymbol{y}_{eq}$.

Root	(z_1, z_2) or (y_1, y_2)	(λ_s, λ_f)	Type
R_1	$(24.944, 0.0176)$	$(-8.186 \times 10^6, -9.296 \times 10^9)$	Sink
R_2	$(-15.451, 15.451)$	$(6.215 \times 10^9, -7.052 \times 10^{12})$	Saddle
R_3	$(25, 6.526 \times 10^{-8})$	$(4.138 \times 10^6, -4.590 \times 10^6)$	Saddle
I_1	$(0, -0.382)$	$(-3.806 \times 10^6, -3.803 \times 10^6)$	Sink
I_2	$(0, 1.002)$	$(7.351 \times 10^3, -7.356 \times 10^3)$	Saddle

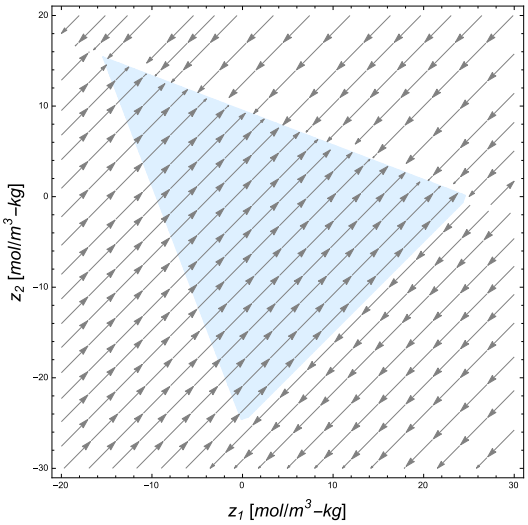

Figure 4.1: Phase flow in reduced space $\boldsymbol{\Xi}$. The blue region is the physically realizable space, i.e. $\boldsymbol{\psi}(\boldsymbol{z}) > 0$. The reaction mechanism are clusters 1 and 2 in table A.1.

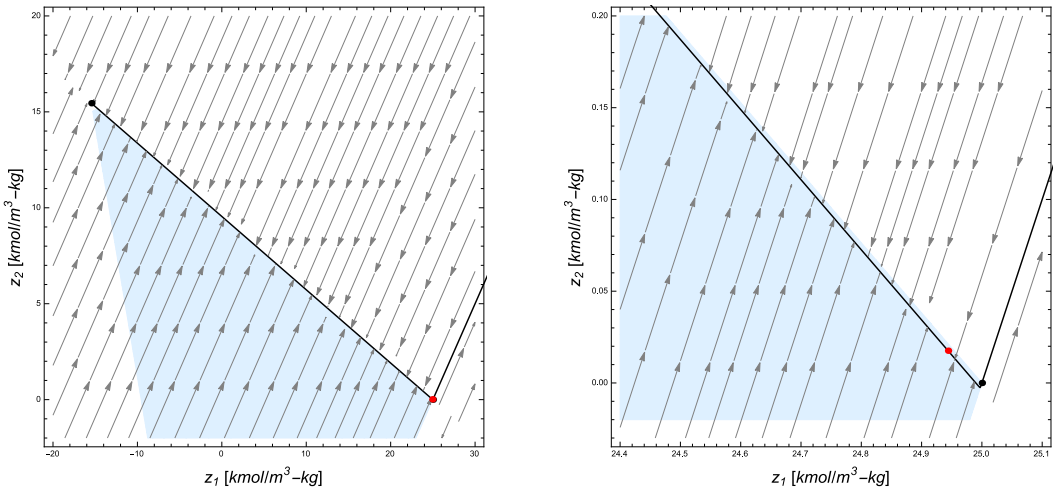

Figure 4.2: Slow invariant manifold for a homogeneous discharge in Ar for $E/N = 27.13$ Td. The reaction mechanism are clusters 1 and 2 in table A.1.

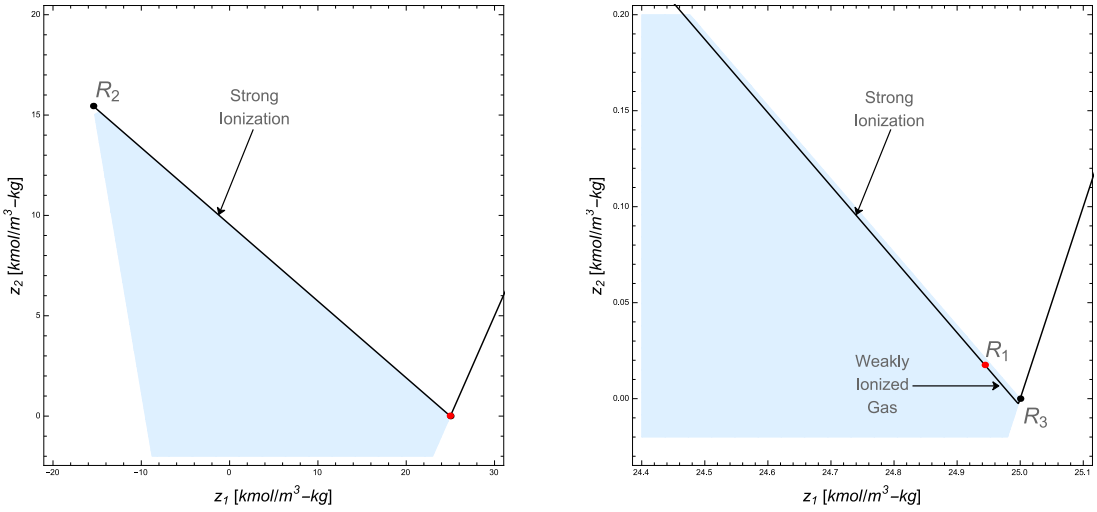

Figure 4.3: SIM structure for a homogeneous discharge in Ar. This structure is prevalent for a moderate range of reduced fields. The reaction mechanism are clusters 1 and 2 in table A.1.

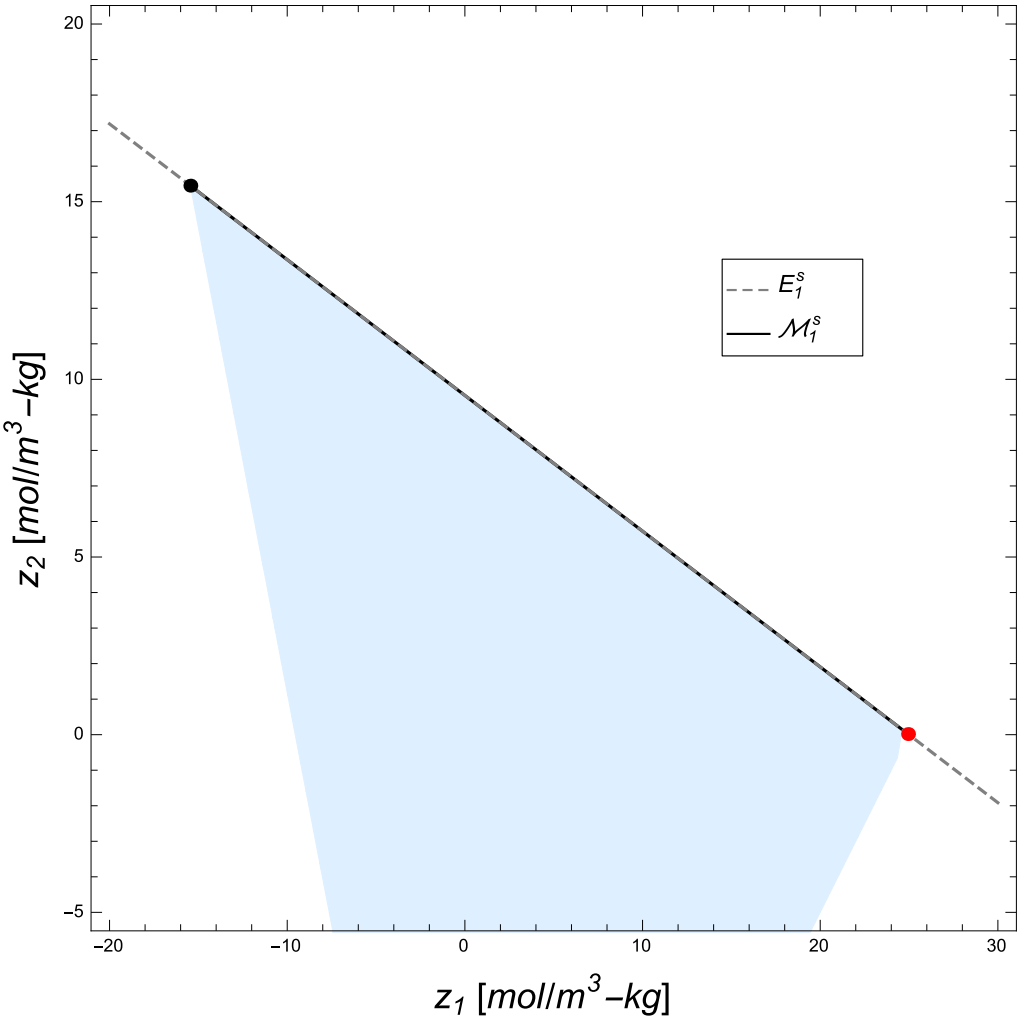

Figure 4.4: 1D SIM (upper branch only) and the slowest eigenspace of both R_1 and R_2. The upper branch of the manifold behaves linearly.

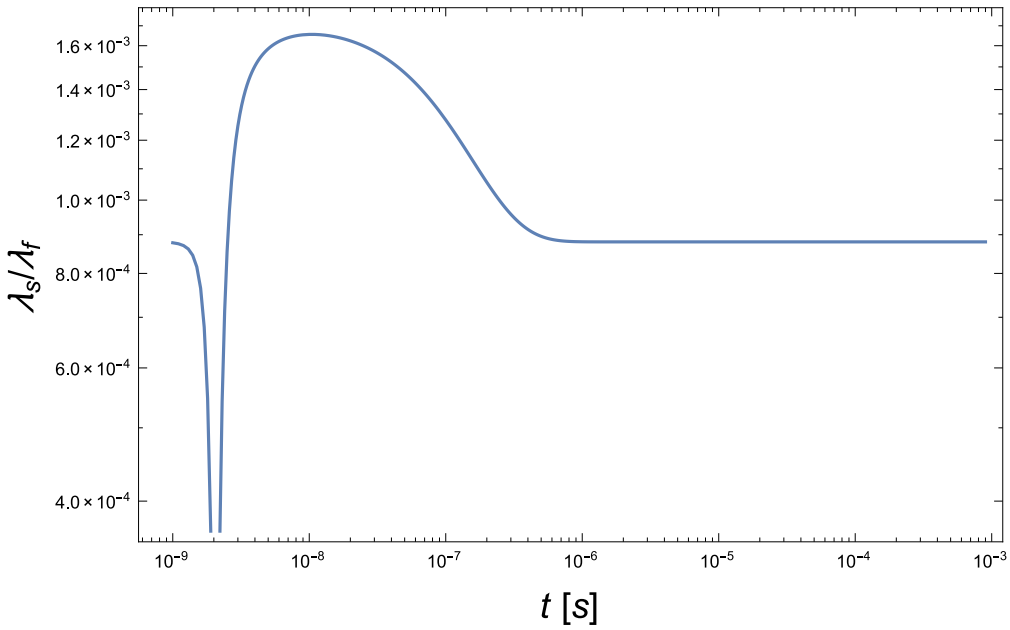

Figure 4.5: Eigenvalue ratio along the upper branch of the SIM.

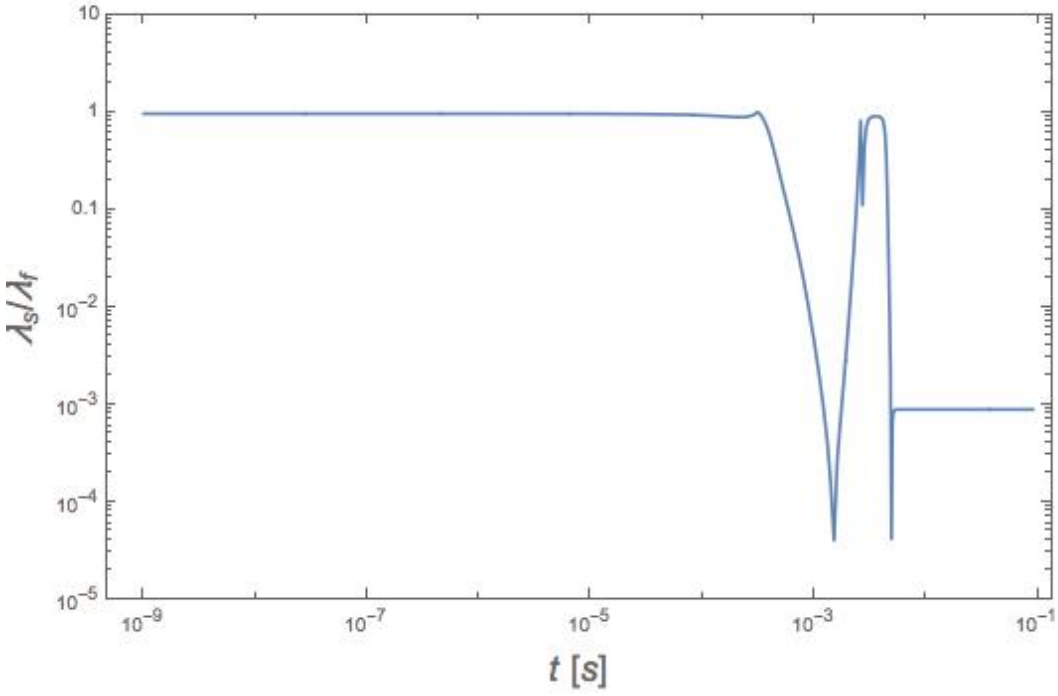

Figure 4.6: Eigenvalue ratio along the lower branch of the SIM.

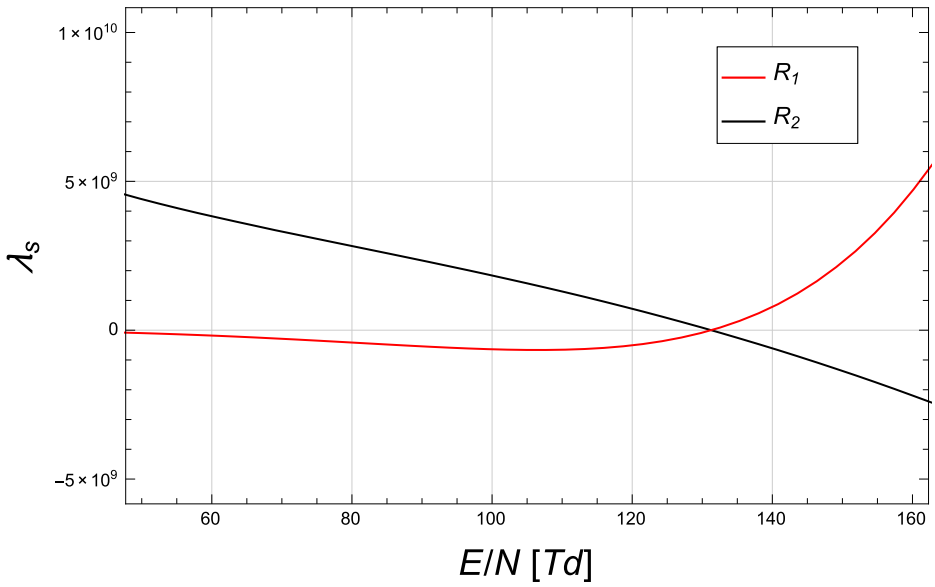

Figure 4.7: Slowest eigenvalue of $\boldsymbol{f}_{\boldsymbol{z}}$ at both R_1 and R_2. Plasma runaway occurs when the slowest eigenvalue of unphysical state R_2 becomes negative and R_1 becomes a saddle.

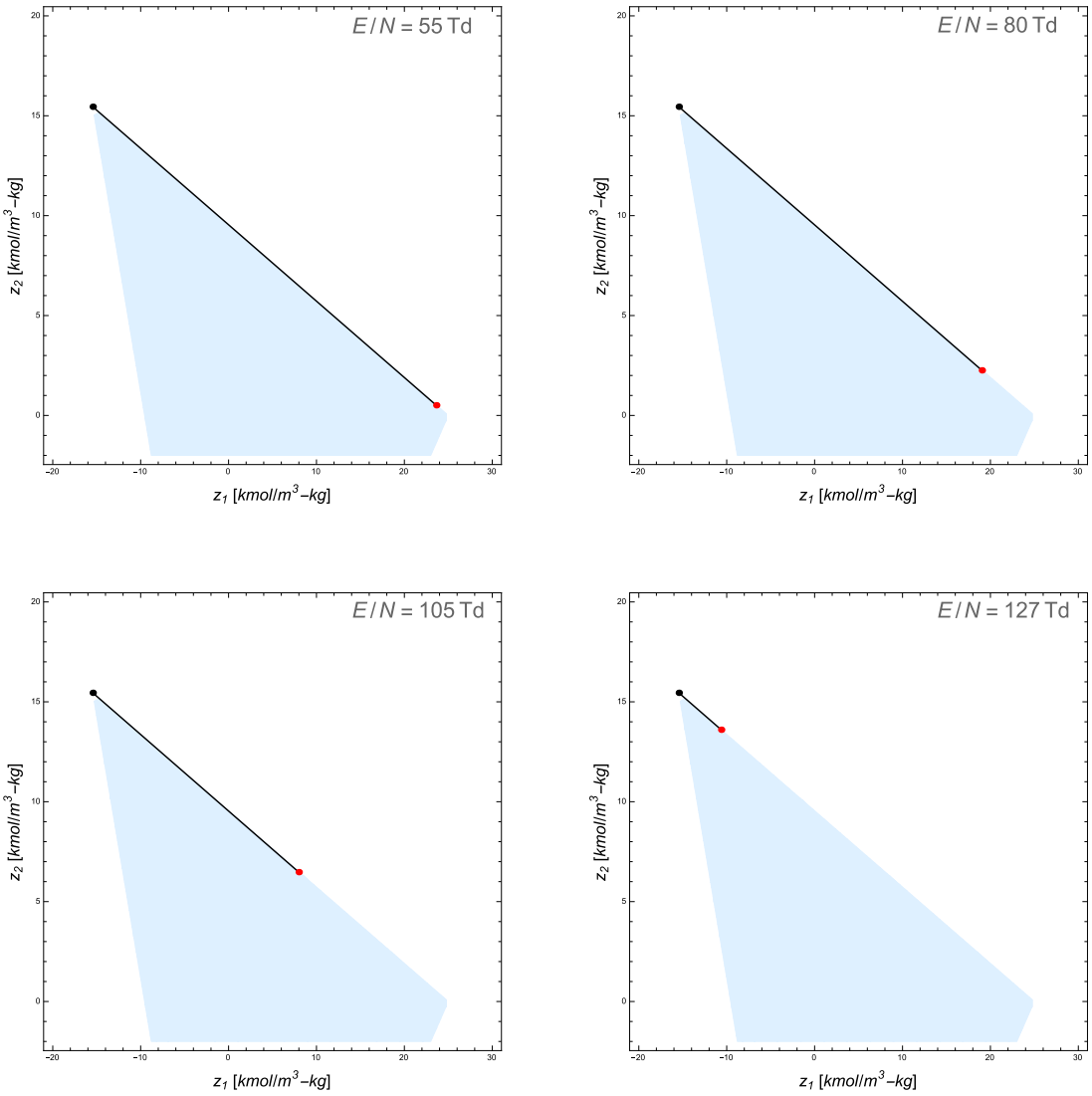

Figure 4.8: Different manifolds for the same system subject to increasing reduced fields E/N. While sink R_1 shifts along phase space, saddle R_2 remains fixed.

4.2 ILDM of Noble Gas Electrical Discharges

This section shows the one-dimensional ILDM of two Ar systems of increasing complexity. The first system comprises clusters 1 and 2 of table A.1 and its behavior is already well-known from the previous section. The second system is all of table A.1, i.e. clusters 1 through 3, whose evolution and eigenspectra under a constant electric field $E/N = 27.13$ Td are shown in fig. 3.8 and 3.11. As expected, the 1D ILDM, bounded by physical constraints, matches the 1D SIM. Starting from physical equlibrium, it tracks the high and low ionization branches until the edge of physical space. The ILDM's upper branch is parametrized by $\theta = z_2$, while the lower branch is parametrized by $\theta = z_1$. Recall that there is no physical meaning for the parametrization choice.

The ILDM of the larger system shows a qualitatively similar structure. It consists of a linear high ionization branch and a considerably smaller nonlinear weak ionization region. This weakly ionized gas branch is not as extensive as that of the smaller Ar system modeled by clusters 1 and 2 because it is embedded in a 2D ILDM. The manifold is shown in fig. 4.10. Since the timescale separation does not span one order of magnitude even, the ILDM will substantially deviate from the SIM. By finding the roots of the reduced source term, it is clear that the linear branch of the ILDM tends toward a saddle $R_2 = (-2.026, 25.206, -22, 567)$, while the smaller nonlinear weak ionization branch tends toward a saddle $R_3 = (25, 4.374 \times 10^{-7}, 3.289 \times 10^{-8})$ [67].

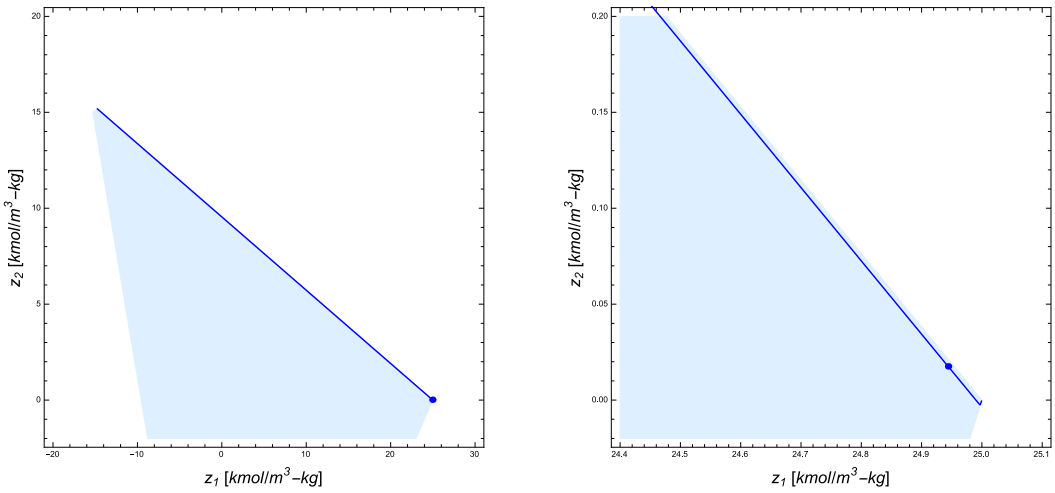

Figure 4.9: ILDM of an Ar discharge at $E/N = 27.13$ Td. The marker indicates physical equlibrium.

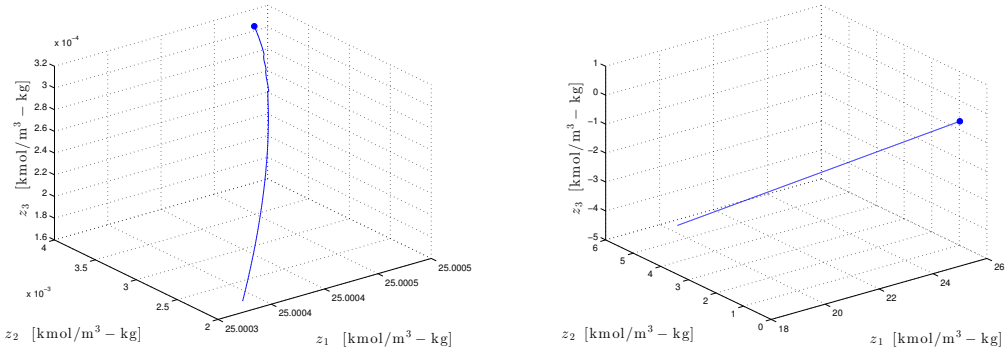

Figure 4.10: ILDM for Ar discharge mechanism in table A.1. Left: Upper branch of the manifold corresponding to high ionization. Right: lower branch of the manifold corresponding to weak ionization.

CHAPTER 5

CONCLUSIONS AND FUTURE WORK

This work has focused on reduced-order models of detailed kinetics for electrical gas discharges in noble gases. Starting from the mathematical modeling of chemical kinetics, a linear subspace where a mixture composition evolves was identified and the appropriate linear transformation to access it was provided based on the problem's conservation constraints. This was followed by the mathematical background and numerical implementation of two popular dimension reduction techniques which have been extensively used in combustion modeling and simulation and had yet to be exploited in plasma-flow solvers. The appropriate modeling of nonequilibrium electrical discharges was also shared and tested for both noble gases and air-like mixtures. Local timescale analysis is a key component of both methods, such that extensive use of linear algebra packages was required to perform invariant subspace, eigen and Schur decompositions, as well as other operations, throughout this work. The results show interesting and useful phenomena that indicate that reduce-order modeling of gas discharges could be applicable to full CFD simulations and coupled to transport phenomena. Furthermore, a bifurcation analysis with the reduced field as the variation parameter was carried out with satisfying results. Electron runaway behaves like an explosion, and this could potentially help studying ignition assistance.

The techniques outlined here were also partially applied to the N_2 mechanism found in table A.2. Despite the correct determination of all of the system's critical

points, this analysis was not successful however, as the algorithms were not able to resolve a small region close to physical equilibrium. It is known that the ILDM method performs poorly in regions where the corresponding eigenspectra includes complex eigenvalues and that may be the reason behind this method's inability to resolve the aforementioned troublesome region. It is still however not known why the 1D SIM method fails, as it appears that the generated orbit meets a singularity on its way to physical equilibrium. Future work will partly consist on identifying the problem and constructing both manifolds. Finally, in order to study plasma-assisted ignition, it is desired to couple ISAT [68], a tabulation storage-retrieval code, and ZDPlasKin [69], a zero-dimensional plasma solver with an integrated BOLSIG+ module, and integrate them to a full CFD plasma-flow solver with AMR framework.

APPENDIX A

DISCHARGE MECHANISMS

Table A.1: Argon discharge chemistry system. Two-body and three-body rate coefficients are given in m^3s^{-1} and m^6s^{-1} respectively.

No.	Reaction	Rate Coefficient	Ref.
(1.1)	$Ar + e^- \rightarrow Ar^+ + e^- + e^-$	BOLSIG+	[56]
(1.2)	$Ar + Ar^+ + e^- \rightarrow Ar + Ar$	$8.50 \times 10^{-39}\ T_e^{-4.5}$	[69]
(2.1)	$Ar + e^- \rightarrow Ar^\star + e^-$	BOLSIG+	[56]
(2.2)	$Ar^\star + e^- \rightarrow Ar + e^-$	$2.00 \times 10^{-13}\ T_e \exp(-2.70/T_e)$	[70]
(2.3)	$Ar^\star + e^- \rightarrow Ar^+ + e^- + e^-$	$1.16 \times 10^{-16}\ T_e^3 \exp(-4.16/T_e)$	[70]
(2.4)	$Ar^\star + Ar + Ar \rightarrow Ar + Ar + Ar$	1.40×10^{-44}	[69]
(3.1)	$Ar_2^+ + e^- \rightarrow Ar + Ar^\star$	$8.50 \times 10^{-13}\ T_e^{-0.67}$	[69]
(3.2)	$Ar + Ar_2^+ \rightarrow Ar + Ar + Ar^+$	$6.00 \times 10^{-12}\ T_g^{-1}$	[69]
(3.3)	$Ar^\star + Ar^\star \rightarrow Ar_2^+ + e^-$	6.00×10^{-16}	[69]
(3.4)	$Ar + Ar + Ar^+ \rightarrow Ar + Ar_2^+$	2.20×10^{-43}	[69]

Table A.2: Nitrogen discharge chemistry system. Two-body and three-body rate coefficients are given in m^3s^{-1} and m^6s^{-1} respectively.

No.	Reaction	Rate Coefficient	Ref.
(01)	$N_2 + e^- \rightarrow N_2(\mathrm{A}, \mathrm{V} = 0-4) + e^-$	BOLSIG+	[56]
(02)	$N_2 + e^- \rightarrow N_2(\mathrm{A}, \mathrm{V} = 5-9) + e^-$	BOLSIG+	[56]
(03)	$N_2 + e^- \rightarrow N_2(\mathrm{A}, \mathrm{V} = 10) + e^-$	BOLSIG+	[56]
(04)	$N_2 + e^- \rightarrow N_2(B) + e^-$	BOLSIG+	[56]
(05)	$N_2 + e^- \rightarrow N_2(C) + e^-$	BOLSIG+	[56]
(06)	$N_2 + e^- \rightarrow N_2(a') + e^-$	BOLSIG+	[56]
(07)	$N_2 + e^- \rightarrow N_2^+ + e^- + e^-$	BOLSIG+	[56]
(08)	$N_2 + N^+ + e^- \rightarrow N + N_2$	$6.00 \times 10^{-39}(T_e/300)^{-1.50}$	[69]
(09)	$N_2^+ + e^- \rightarrow N + N$	$1.80 \times 10^{-13}(T_e/300)^{-0.39}$	[69]
(10)	$N3^+ + e^- \rightarrow N + N_2$	$2.00 \times 10^{-13}(T_e/300)^{-0.50}$	[69]
(11)	$N4^+ + e^- \rightarrow N_2 + N_2$	$2.30 \times 10^{-12}(T_e/300)^{-0.53}$	[69]
(12)	$N_2 + N_2 + N^+ \rightarrow N_2 + N3^+$	$1.70 \times 10^{-41}(T_{eff}/300)^{-2.10}$	[69]
(13)	$N + N_2^+ \rightarrow N_2 + N^+$	$7.20 \times 10^{-19}(T_{eff}/300)$	[69]
(14)	$N + N_2 + N_2^+ \rightarrow N_2 + N3^+$	$9.00 \times 10^{-42}\exp(400/T_{eff})$	[69]
(15)	$N_2 + N_2 + N_2^+ \rightarrow N_2 + N4^+$	$5.90 \times 10^{-41}(T_{eff}/300)^{-2.20}$	[69]
(16)	$N_2 + N4^+ \rightarrow N_2 + N_2 + N_2^+$	$2.10 \times 10^{-22}\exp(T_{eff}/120)$	[69]
(17)	$N_2(A) \rightarrow N_2$	5.0e-01	[69]
(18)	$N_2(B) \rightarrow N_2(A)$	1.0e+05	[69]
(19)	$N_2(a') \rightarrow N_2$	1.0e+02	[69]
(20)	$N_2(C) \rightarrow N_2(B)$	2.5e+07	[69]
(21)	$N_2(A) + N_2(a') \rightarrow N4^+ + e^-$	4.0e-12	[69]
(22)	$N_2(a') + N_2(a') \rightarrow N4^+ + e^-$	4.0e-11	[69]
(23)	$N_2(A) + N_2^+ \rightarrow N + N3^+$	3.0e-10	[69]
(24)	$N + N3^+ \rightarrow N_2 + N_2^+$	6.6e-11	[69]
(25)	$N + N4^+ \rightarrow N_2 + N_2 + N^+$	1.0e-11	[69]
(26)	$N + N_2(A) \rightarrow N + N_2$	2.0e-12	[69]
(27)	$N_2 + N_2(A) \rightarrow N_2 + N_2$	3.0e-16	[69]
(28)	$N_2(A) + N_2(A) \rightarrow N_2 + N_2(B)$	3.0e-10	[69]
(29)	$N_2(A) + N_2(A) \rightarrow N_2 + N_2(C)$	1.5e-10	[69]
(30)	$N_2 + N_2(B) \rightarrow N_2 + N_2$	2.0e-12	[69]
(31)	$N_2 + N_2(B) \rightarrow N_2 + N_2(A)$	3.0e-11	[69]
(32)	$N_2 + N_2(a') \rightarrow N_2 + N_2(B)$	1.9e-13	[69]
(33)	$N_2 + N_2(C) \rightarrow N_2 + N_2(a')$	1.0e-11	[69]
(34)	$N + N_2 + N^+ \rightarrow N_2 + N_2^+$	1.0e-29	[69]
(35)	$N + N + N_2 \rightarrow N_2 + N_2(A)$	1.7e-33	[69]
(36)	$N + N + N_2 \rightarrow N_2 + N_2(B)$	2.4e-33	[69]

APPENDIX B

ILDM MATLAB IMPLEMENTATION

```
function X = ILDM(x,n,i,stp,dir,maxiter)

    PlasmaParameters;

    % Function ILDM : Computes ILDM for F(x)
    % I (x)   : Equilibrium Point
    % I (n)   : ILDM-dim
    % I (i)   : Reaction Progress Variables Indices
    % I (stp) : Initial Continuation Process Step Size
    % O (X)   : Parametrized Manifold

    X = [x'];

    [F,J]     = source(x);
    [ZR,ZL,D] = rschur(J,n);
    [P,d] = parametrize(n,i,dir);
    [ZRS,ZRF,ZLS,ZLF] = split(ZR,ZL,n);

    for( j = 1:maxiter )

        [xp,vt] = predictor(x,ZRS,P,d,stp);
        [xc,flag] = corrector(xp,n,P);
        [bound,stp] = checkBoundaries(xc,stp);

        if (bound)
            disp([j])
            disp([x vt xp xc])
            disp('')

            x = xc;
```

```
            [F,J]     = source(x);
            [ZR,ZL,D] = rschur(J,n);
            [P,d] = parametrize(n,i,dir);
            [ZRS,ZRF,ZLS,ZLF] = split(ZR,ZL,n);

            X = [X;x'];

        end

    end

end

%% Continuation Process
%  [1] Predictor
%  [2] Corrector
%  [3] Boundary Check
%
function [xp,vt] = predictor(x,ZRS,P,d,stp)

    PlasmaParameters;

    % Function parametrize : Finds Tangent Vector & Predicted Point
    % I (x)   : State Vector
    % I (ZRS) : Right-Slow-Invariant Matrix
    % I (stp) : Step Size
    % O (xp)  : Predicted Manifold Point
    % O (vt)  : Predictor (Tangent Vector)

    % Tangent Vector (Not Normalized)
    vt = stp*ZRS*((P*ZRS)\d);
```

```
    % Predicted Point
    xp = x + vt;

end

function [xc,flag] = corrector(xp,n,P)

    par.xp = xp;
    par.n  = n;
    par.P  = P;

    load varscale.mat;
    xs = varscale;

    rtol = 1E-2;
    opt = [];
    wk  = [];

    [xc,info,~] = nleq1(@manifold,xp,xs,rtol,opt,par,wk);

    flag = info.ierr;

end

function [bound,stp] = checkBoundaries(xc,stp)

    PlasmaParameters;

    % Function checkBoundaries : Check Boundedness of Solution
    % I (xc) : Corrected Point
```

```
    y = xo + MT*L*xc;

    if ( sum(y < 0) > 0 )
        stp = (1E-2)*stp;
        bound = false;
    else

        bound = true;
    end

end

%% Functions & Jacobians
%  [1] Parametrization
%  [2] Manifold Equations & Jacobian
%  [3] Chemistry Source & Jacobian
%
function [P,d] = parametrize(n,i,dir)

    PlasmaParameters;

    % Function parametrize : Sets Up Param. Equations & Direction
       Vector
    % I (n) : ILDM-dim
    % I (i) : Reaction Progress Variables Indices

    IP = eye(nvars);
    ID = eye(n);
    P = zeros(n,nvars);
    d = zeros(1,n);
```

```
    % Conservation of Mass Parametrization
    % P(1:nelem,:) = A;
    % Reaction Progress Parametrization
    P(n,:) = IP(i,:);

    % Direction Vector
    d = dir*ID(:,n);

end
%
function [out,fail] = manifold(x,flag,par)

    PlasmaParameters;

    % Function manifold : Computes the Manifold Equations
    % I (x)  : Newton Iterate
    % I (xp) : Predicted Manifold Point
    % I (n)  : ILDM-dim
    % I (P)  : Parametrization Matrix

    xp = par.xp;
    n  = par.n;
    P  = par.P;

    [F,J] = source(x);
    [ZR,ZL] = rschur(J,n);
    [~,~,~,ZLF] = split(ZR,ZL,n);

    if ( strcmpi('',flag) )
```

```
        GF = [ ZLF*F ; P*(x - xp) ];

        out = GF;
        fail = 0;

    else ( strcmp('jacobian',flag) )

        GJ = [ ZLF*J ; P ];

        out = GJ;
        fail = 0;

    end

end
%
function [F,J] = source(x,varargin)

    % Function source : Chemical Source Term
    % I (x) : State Vector (Chemical Concentration)
    % O (F) : Chemical Source Term
    % O (J) : Chemical Jacobian

    % Variable Input Argument List
    % varargin : Empty

    PlasmaParameters;
    Te = 3.8827 * eV;
    Te = Te/eV;

    % Physical Space
```

```
x = xo + MT*L*x;
x = NA*x;

% Reaction Rates [m^-3 s^-1]
ratecoef = zeros(nreac,1);
rates    = zeros(nreac,1);
jacrates = zeros(nreac,nspec);

for r = 1:nreac

    Coef = reacRateCoef(r,:);

    if (Coef(1) == 0)

        Coef = Coef(2:end);
        Tep = Te*ones(size(Coef'));
        Tep = (1./Tep).^((0:6)');
        ratecoef(r) = exp(Coef*Tep);

    else

        Coef = Coef(2:end);
        A = Coef(1);
        B = Coef(2);
        C = Coef(3);
        E = Coef(4);

        ratecoef(r) = A*((Te/B)^C)*exp(E/Te);

    end
```

```
    R = reactant(r,:);
    R = R';
    S = x(1:eindex);
    rates(r) = ratecoef(r)*prod(S.^R);

    for (s = 1:nspec)

        R = reactant(r,:);
        R = R';
        R(s) = R(s) - 1;
        if (R(s) == -1)
            jacrates(r,s) = 0;
        else
            jacrates(r,s) = (R(s)+1)*ratecoef(r)*prod(S.^R);
        end

    end

end

% Reaction Source Terms [m^-3 s^-1]
F = zeros(nspec,1);
J = zeros(nspec,nspec);

F = netReac*rates;
J = netReac*jacrates;

F = F./NA;

F = D*F;
J = D*J*L;
```

```
    F = F/MT;

end

%% Linear Algebra
%  [1] Invariant Decomposition
%  [2] Split
%
function [ZR,ZL,D] = rschur(J,n)

    PlasmaParameters;

    % Function rschur : Orders Schur Decomposition
    % Re(eigv(J)) in Descending Order
    % I (J)  : Chemical Jacobian
    % O (ZR) : Right-Invariant Matrix
    % O (ZL) : Left-Invariant
    % O (D)  : Block-Triangular Invariant Matrix

    [Q,T] = schur(J);

    ilst = 1;

for ( i = 1:nvars )

    ifst = ilst;

    for ( j = ilst+1:nvars )
        if ( T(j,j) > T(ifst,ifst) )
            ifst = j;
```

```
        end
    end

    if ( ifst ~= ilst)
        C = lapack('dtrexc','V',nvars,T,nvars,Q,nvars,...
                   ifst,ilst,zeros(nvars,1),0);

        [T,Q] = C{[3,5]};
    end

    ilst = ilst + 1;

end

    TS  = T(1:n,1:n);
    TF  = T(n+1:nvars,n+1:nvars);
    TSF = T(1:n,n+1:nvars);

    X = lyap(TS,-TF,TSF);
    XR = eye(nvars);
    XL = eye(nvars);

    XR(1:n,n+1:nvars) =  X;
    XL(1:n,n+1:nvars) = -X;

    ZR = Q*XR;
    ZL = XL*Q';

    D = zeros(nvars,nvars);
    D(1:n,1:n) = TS;
    D(n+1:nvars,n+1:nvars) = TF;
```

```
end
%
function [ZRS,ZRF,ZLS,ZLF] = split(ZR,ZL,n)

    PlasmaParameters;

    % Function split : Splits Invariant Matrices
    % I (ZR)  : Right-Invariant Matrix
    % I (ZL)  : Left-Invariant Matrix
    % O (ZRS) : Right-Slow-Invariant Block
    % O (ZRF) : Right-Fast-Invariant Block
    % O (ZLS) : Left-Slow-Invariant Block
    % O (ZLF) : Left-Fast-Invariant Block

    ZRS = ZR(:,1:n);
    ZRF = ZR(:,n+1:nvars);

    ZLS = ZL(1:n,:);
    ZLF = ZL(n+1:nvars,:);

end
```

REFERENCES

[1] U. Maas and S. B. Pope, "Simplifying chemical kinetics: intrinsic low-dimensional manifolds in composition space," *Combustion and Flame*, vol. 88, no. 3, pp. 239–264, 1992.

[2] S. Singh, "Rational reduction of reactive flow models and efficient computation of their solutions," Ph.D. dissertation, University of Notre Dame, 2003.

[3] Z. Ren and S. B. Pope, "The use of slow manifolds in reactive flows," *Combustion and flame*, vol. 147, no. 4, pp. 243–261, 2006.

[4] M. Denison and L. Massa, "On gasdynamic instabilities supported by non-equilibrium plasma in a supersonic flow," in *6th AIAA Flow Control Conference*, no. AIAA-2012-2737, June 2012.

[5] A. Greig, C. H. Birzer, and M. Arjomandi, "Atmospheric plasma thruster: Theory and concept," *AIAA journal*, vol. 51, no. 2, pp. 362–371, 2012.

[6] S. B. Leonov and D. A. Yarantsev, "Plasma-induced ignition and plasma-assisted combustion in high-speed flow," *Plasma Sources Science and Technology*, vol. 16, no. 1, p. 132, 2007.

[7] S. Leonov, A. Firsov, Y. Isaenkov, M. Shurupov, D. Yarantsev, and M. Shneider, "Plasma-based fast mixing and ignition in supersonic flow," in *17th AIAA International Space Planes and Hypersonic Systems and Technologies Conference, no. AIAA*, vol. 2327, 2011.

[8] S. Roy, K. Singh, and D. V. Gaitonde, "Air plasma actuators for effective flow control," in *45th AIAA Aerospace Sciences Meeting and Exhibit*, 2007, pp. 8–11.

[9] Z. Chen, L. Hao, and B. Zhang, "A model for nanosecond pulsed dielectric barrier discharge (nsdbd) actuator and its investigation on the mechanisms of separation control over an airfoil," *Science China Technological Sciences*, vol. 56, no. 5, pp. 1055–1065, 2013.

[10] M. Nishihara, K. Takashima, J. Rich, and I. Adamovich, "Mach 5 bow shock control by a nanosecond pulse surface dielectric barrier discharge," *Physics of Fluids (1994-present)*, vol. 23, no. 6, p. 066101, 2011.

[11] J. Shang and P. Huang, "Surface plasma actuators modeling for flow control," *Progress in Aerospace Sciences*, vol. 67, pp. 29–50, 2014.

[12] V. Soloviev and V. Krivtsov, "Surface barrier discharge modelling for aerodynamic applications," *Journal of Physics D: Applied Physics*, vol. 42, no. 12, p. 125208, 2009.

[13] J.-J. Wang, K.-S. Choi, L.-H. Feng, T. N. Jukes, and R. D. Whalley, "Recent developments in dbd plasma flow control," *Progress in Aerospace Sciences*, vol. 62, pp. 52–78, 2013.

[14] T. Corke, M. Post, and D. Orlov, "Sdbd plasma enhanced aerodynamics: concepts, optimization and applications," *Progress in Aerospace Sciences*, vol. 43, no. 7-8, pp. 193–217, 2007.

[15] C. Y. Schuele, T. C. Corke, and E. Matlis, "Control of stationary cross-flow modes in a mach 3.5 boundary layer using patterned passive and active roughness," *Journal of Fluid Mechanics*, vol. 718, pp. 5–38, 2013.

[16] M. Denison, E. Cisneros, and L. Massa, "Compressibility effects on dielectric barrier discharge actuation and boundary layer receptivity," 2014.

[17] J. Poggie, "Role of charged particle inertia in pulsed electrical discharges," *AIAA Paper*, vol. 1195, 2010.

[18] M. F. Denison, "Compressibility effects on the non-linear receptivity of boundary layers to dielectric barrier discharges," 2013.

[19] C. A. Eckett, "Numerical and analytical studies of the dynamics of gaseous detonations," Ph.D. dissertation, Citeseer, 2000.

[20] M. H. Wilcoxson and V. I. Manousiouthakis, "Simulation of a three-moment fluid model of a two-dimensional radio frequency discharge," *Chemical engineering science*, vol. 51, no. 7, pp. 1089–1106, 1996.

[21] J. Shang, "Surface direct current discharge for hypersonic flow control," *Journal of Spacecraft and Rockets*, vol. 45, no. 6, pp. 1213–1222, 2008.

[22] S. Roy and D. V. Gaitonde, "Force interaction of high pressure glow discharge with fluid flow for active separation control," *Physics of Plasmas (1994-present)*, vol. 13, no. 2, p. 023503, 2006.

[23] I. Kossyi, A. Y. Kostinsky, A. Matveyev, and V. Silakov, "Kinetic scheme of the non-equilibrium discharge in nitrogen-oxygen mixtures," *Plasma Sources Science and Technology*, vol. 1, no. 3, p. 207, 1992.

[24] S. Pancheshnyi and A. Y. Starikovskii, "Two-dimensional numerical modelling of the cathode-directed streamer development in a long gap at high voltage," *J. Phys. D: Appl. Phys*, vol. 36, pp. 2683–2691, 2003.

[25] J. Poggie, I. Adamovich, N. Bisek, and M. Nishihara, "Numerical simulation of nanosecond-pulse electrical discharges," *Plasma Sources Science and Technology*, vol. 22, no. 1, p. 015001, 2013.

[26] S. Mahadevan and L. L. Raja, "Simulations of direct-current air glow discharge at pressures 1 torr: Discharge model validation," *Journal of Applied Physics*, vol. 107, no. 9, p. 093304, 2010.

[27] D. Tsyganov and S. Pancheshnyi, "Simulation of n-atom production in dielectric-barrier discharge in nitrogen at atmospheric pressure," *Plasma Sources Science and Technology*, vol. 21, no. 6, pp. 65 010–65 017, 2012.

[28] M. Castillo, I. Méndez, A. Islyaikin, V. J. Herrero, and I. Tanarro, "Low-pressure dc air plasmas. investigation of neutral and ion chemistry," *The Journal of Physical Chemistry A*, vol. 109, no. 28, pp. 6255–6263, 2005.

[29] M. Capitelli, C. M. Ferreira, A. I. Osipov, and B. F. Gordiets, *Plasma kinetics in atmospheric gases*. Springer, 2000.

[30] S. Lam and D. Coussis, "Understanding complex chemical kinetics with computational singular perturbation," in *Symposium (International) on Combustion*, vol. 22, no. 1. Elsevier, 1989, pp. 931–941.

[31] U. Maas and D. Schmidt, "Analysis of the intrinsic low-dimensional manifolds of strained and unstrained flames," in *3rd Workshop on Modelling of Chemical Reaction Systems, Heidelberg*, 1996.

[32] P. K. Jha and C. P. Groth, "Tabulated chemistry approaches for laminar flames: Evaluation of flame-prolongation of ildm and flamelet methods," *Combustion Theory and Modelling*, vol. 16, no. 1, pp. 31–57, 2012.

[33] S. Gupta, H. G. Im, and M. Valorani, "Classification of ignition regimes in hcci combustion using computational singular perturbation," *Proceedings of the Combustion Institute*, vol. 33, no. 2, pp. 2991–2999, 2011.

[34] J. Nafe and U. Maas, "Hierarchical generation of ildms of higher hydrocarbons," *Combustion and flame*, vol. 135, no. 1, pp. 17–26, 2003.

[35] V. Bykov and U. Maas, "Hierarchy analysis and reduction of reacting flow systems," in *Computational Science and High Performance Computing IV*. Springer, 2011, pp. 233–252.

[36] Z. Ren, S. B. Pope, A. Vladimirsky, and J. M. Guckenheimer, "The invariant constrained equilibrium edge preimage curve method for the dimension reduction of chemical kinetics," *The Journal of chemical physics*, vol. 124, no. 11, p. 114111, 2006.

[37] A. N. Al-Khateeb, J. M. Powers, S. Paolucci, A. J. Sommese, J. A. Diller, J. D. Hauenstein, and J. D. Mengers, "One-dimensional slow invariant manifolds for spatially homogenous reactive systems," *The Journal of chemical physics*, vol. 131, no. 2, p. 024118, 2009.

[38] A. Dauwe, M. Tytgadt, D. Reiter, and M. Baelmans, "Automatic reduction of the hydrocarbon reaction mechanisms in fusion edge plasmas," Forschungszentrum Juelich GmbH (Germany). Inst. fuer Plasmaphysik (IPP), Tech. Rep., 2006.

[39] P. Scheubert, *Modelling and Diagnostics of Low Pressure Plasma Discharges*. Shaker, 2002.

[40] D. Lebiedz, V. Reinhardt, and J. Siehr, "Minimal curvature trajectories: Riemannian geometry concepts for slow manifold computation in chemical kinetics," *Journal of Computational Physics*, vol. 229, no. 18, pp. 6512–6533, 2010.

[41] U. Maas, "Efficient calculation of intrinsic low-dimensional manifolds for the simplification of chemical kinetics," *Computing and Visualization in Science*, vol. 1, no. 2, pp. 69–81, 1998.

[42] J. M. Powers, S. Paolucci, and J. D. Mengers, "The slowness of invariant manifolds constructed by connection of heteroclinic orbits."

[43] E. N. Lorenz and V. Krishnamurthy, "On the nonexistence of a slow manifold," *Journal of the Atmospheric Sciences*, vol. 44, no. 20, pp. 2940–2950, 1987.

[44] F. Creta, A. Adrover, S. Cerbelli, M. Valorani, and M. Giona, "Slow manifold structure in explosive kinetics. 1. bifurcations of points-at-infinity in prototypical

models," *The Journal of Physical Chemistry A*, vol. 110, no. 50, pp. 13 447–13 462, 2006.

[45] M. Giona, A. Adrover, F. Creta, and M. Valorani, "Slow manifold structure in explosive kinetics. 2. extension to higher dimensional systems," *The Journal of Physical Chemistry A*, vol. 110, no. 50, pp. 13 463–13 474, 2006.

[46] L. Perko, *Differential equations and dynamical systems*, ser. Texts in applied mathematics. Springer-Verlag, 2001.

[47] A. N. S. Al-Khateeb, "Fine scale phenomena in reacting systems: identification and analysis for their reduction," Ph.D. dissertation, University of Notre Dame, 2010.

[48] J. van Oijen, *Flamelet-generated manifolds: development and application to premixed laminar flames*. Technische Universiteit Eindhoven, 2002.

[49] M. J. Davis and R. T. Skodje, "Geometric investigation of low-dimensional manifolds in systems approaching equilibrium," *The Journal of chemical physics*, vol. 111, no. 3, pp. 859–874, 1999.

[50] P. Hung, "Algorithms for reaction mechanism reduction and numerical simulation of detonations initiated by projectiles," Ph.D. dissertation, California Institute of Technology, 2003.

[51] U. Maas and S. B. Pope, "Implementation of simplified chemical kinetics based on intrinsic low-dimensional manifolds," in *Symposium (International) on Combustion*, vol. 24, no. 1. Elsevier, 1992, pp. 103–112.

[52] V. Bykov and U. Maas, "The extension of the ildm concept to reaction–diffusion manifolds," *Combustion Theory and Modelling*, vol. 11, no. 6, pp. 839–862, 2007.

[53] A. C. Hindmarsh and R. Serban, "User documentation for cvodes v2. 7.0," 2012.

[54] P. Colella, D. Graves, T. Ligocki, D. Martin, D. Modiano, D. Serafini, and B. Van Straalen, "Chombo software package for amr applications-design document," 2000.

[55] E. Anderson, Z. Bai, C. Bischof, S. Blackford, J. Demmel, J. Dongarra, J. Du Croz, A. Greenbaum, S. Hammerling, A. McKenney, *et al.*, *LAPACK Users' guide*. Siam, 1999, vol. 9.

[56] G. Hagelaar and L. Pitchford, "Solving the boltzmann equation to obtain electron transport coefficients and rate coefficients for fluid models," *Plasma Sources Science and Technology*, vol. 14, no. 4, p. 722, 2005.

[57] C. Yamabe, S. Buckman, and A. Phelps, "Measurement of free-free emission from low-energy-electron collisions with ar," *Physical Review A*, vol. 27, no. 3, p. 1345, 1983.

[58] A. Phelps and L. Pitchford, "Anisotropic scattering of electrons by n 2 and its effect on electron transport," *Physical Review A*, vol. 31, no. 5, p. 2932, 1985.

[59] Phelps database. [Online]. Available: www.lxcat.net

[60] M. Capitelli, C. Gorse, D. Iasillo, and S. Longo, "Different aspects of self-consistent modeling of non-equilibrium discharges," in *The XXII. international conference on phenomena in ionized gases (ICPIG)*, vol. 363, no. 1. AIP Publishing, 1996, pp. 121–135.

[61] A. J. Sommese and C. W. Wampler, *The Numerical solution of systems of polynomials arising in engineering and science*. World Scientific, 2005, vol. 99.

[62] D. J. Bates, J. D. Hauenstein, A. J. Sommese, and C. W. Wampler, *Numerically solving polynomial systems with Bertini*. SIAM, 2013, vol. 25.

[63] G. H. Golub and C. F. Van Loan, *Matrix computations*. JHU Press, 2012, vol. 3.

[64] Nist standard reference database number 69. [Online]. Available: webbook.nist.gov/chemistry/

[65] Nist-janaf thermochemical tables. [Online]. Available: kinetics.nist.gov/janaf/

[66] W. C. Rheinboldt and J. V. Burkardt, "Algorithm 596: A program for a locally parameterized continuation process," *ACM Trans. Math. Software*, vol. 9, no. 2, pp. 236–241, 1983.

[67] P. J. Schmid, "Dynamic mode decomposition of numerical and experimental data," *Journal of Fluid Mechanics*, vol. 656, pp. 5–28, 2010.

[68] S. Pope, "Computationally efficient implementation of combustion chemistry using in situ adaptive tabulation," 1997.

[69] S. Pancheshnyi, B. Eismann, G. Hagelaar, and L. Pitchford, "Computer code zdplaskin (university of toulouse, laplace, cnrs-ups-inp, toulouse, france, 2008)," *URL http://www. zdplaskin. laplace. univ-tlse. fr*.

[70] J. W. Shon and M. J. Kushner, "Excitation mechanisms and gain modeling of the high-pressure atomic ar laser in he/ar mixtures," *Journal of applied physics*, vol. 75, no. 4, pp. 1883–1890, 1994.

[71] E. Moreau, "Airflow control by non-thermal plasma actuators," *Journal of Physics D: Applied Physics*, vol. 40, p. 605, 2007.

[72] D. Roupassov, A. Nikipelov, M. Nudnova, and A. Y. Starikovskii, "Flow separation control by plasma actuator with nanosecond pulsed-periodic discharge," *AIAA journal*, vol. 47, no. 1, pp. 168–185, 2009.

[73] C. Schuele, "Control of stationary crossflow modes using passive patterned roughness and dbd plasma actuators at mach 3.5," Ph.D. dissertation, University of Notre Dame, September 2011.

[74] A. R. Hoskinson, *Measurements and simulations of surface dielectric barrier discharges used as plasma actuators*, 2009.

[75] R. Fox, *Computational models for turbulent reacting flows.* Cambridge University Press, Cambridge, 2003.

[76] J. C. Keck and D. Gillespie, "Rate-controlled partial-equilibrium method for treating reacting gas mixtures," *Combustion and Flame*, vol. 17, no. 2, pp. 237–241, 1971.

BIOGRAPHICAL STATEMENT

Esteban Cisneros was born in Guadalajara, Mexico, in 1988. He received his B.S. degree in Mechatronics engineering from the Panamerican University, Mexico, in 2007. He is interested in plasma thermochemistry, reactive flow computations and high-speed flow control. Esteban is a student member of the AIAA.